# The geochemistry and geochronology of the Xiarihamu II mafic–ultramafic complex, Eastern Kunlun, Qinghai Province, China: Implications for the genesis of magmatic Ni–Cu sulfide deposits

Bo Peng [a], Fengyue Sun [a,*,1], Bile Li [a], Guan Wang [b], Shijin Li [c], Tuofei Zhao [a], Liang Li [a], Yubo Zhi [a]

[a] College of Earth Sciences, Jilin University, Changchun, 130061, PR China
[b] Sichun Xin Shun Mineral Limited Liability Corporation, Chengdu, 610041, China
[c] Qinghai Geological Survey, Xining 810000, China

## ABSTRACT

The Xiarihamu Ni–Cu deposit of Qinghai Province, China, is located in the central region of the Eastern Kunlun Orogen (EKO), which is bordered by the Qaidam block (QDM) to the north and the Bayan Har-Songanganzi Terrane (BH-SG) to the south. The Xiarihamu region contains four mafic–ultramafic complexes that have intruded Neoproterozoic garnet-bearing granitic gneiss and metamorphic rocks of the Paleoproterozoic Jinshuiko Group. Ni–Cu sulfide ores of economic interest are found within intrusions of these four complexes. The Xiarihamu I intrusion is the main host of the Ni–Cu mineralization. Evidence of strong mineralization is also found in trenches and drill-cores from the Xiarihamu II intrusion. The remaining two intrusions contain little or no mineralization. The economic Ni–Cu ores are bedded or lenticular in nature or occur as localized veins of sulfide minerals. The Hf isotopic compositions of zircons from the two complexes have positive $\varepsilon Hf_{(t)}$ values of 4.0–13.7, indicating that its parental magmas originated from depleted asthenospheric mantle. However, the Xiarihamu II intrusion contains many xenoliths of Neoproterozoic monzogranite, and the samples from both complexes show similar rare earth and trace element patterns, are strongly enriched in lithophile elements (e.g., Rb, Ba, Th, U, and K) and light rare earth elements, and are moderately depleted in Nb, Ta, P, and Ti, indicating significant crustal contamination. Sulfide minerals from the two complexes have $\delta^{34}S$ values of 3.4%–7.6% that lie outside the range of mantle values ($-2\% \pm 2\%$), suggesting that assimilated crustal sulfur was the main contributor to S saturation at the Xiarihamu Ni–Cu deposit. The major and trace element characteristics, and Sr, Nd and Hf isotopic compositions of the two Xiarihamu mafic–ultramafic complexes suggest that they were derived from a common source. A sample of gabbro from the Xiarihamu II mafic–ultramafic complex yields an age of $424 \pm 1$ Ma, which is interpreted as the timing of magmatic crystallization. Considering the tectonic evolution of the region, the complex probably formed in a post-collisional extensional regime.

The parental magma experienced significant crustal contamination, either during ascent or emplacement, triggering S over-saturation that resulted in the precipitation of sulfide minerals, and sulfide enrichment in the magma. The silicate magma continued to ascend due to buoyancy, eventually forming the Xiarihamu mafic–ultramafic complex and the Xiarihamu Ni-Cu sulfide deposit.

## 1. Introduction

The tectonic setting, rock type, rock associations, primary magma, and magma source of magmatic copper and nickel sulfide deposits are generally agreed upon, but the ore-forming processes and metallogenic models for such deposits remain debated. One metallogenic model states that the ore-bearing intrusions represent conduits through which magma ascended (Naldrett, 2004; Barnes and Lightfoot, 2005; Zhang et al., 2009a). In this model, the ore body is located mainly at the base of the intrusion, ore pulp is continuously enriched in the magma conduits, and assimilated crustal sulfur is necessary for metallogenesis. An alternative model proposes that the ore-bearing intrusive rock is actually a terminal magma chamber (Tang et al., 2007) that acts as a storage location for the ore-bearing magma and ore pulp after it has experienced melting away and fractionation in an intermediate magma chamber. The model suggests that the ore forms as pulses of magma move from the intermediate to the terminal magma chamber. The two metallogenic models have significantly different implications for ore-forming processes.

* Corresponding author.
  E-mail addresses: pengbo13@mails.jlu.edu.cn (B. Peng), fengyuesun63@126.com (F. Sun).
[1] Postal address: 2199 Jianshe Street, College of Earth Sciences, Jilin University, Changchun 130061, China.

The Eastern Kunlun Orogen (EKO) belt is a key part of the western portion of the Central Orogenic Belt on mainland China. Since it hosts orogenic gold and porphyry ore deposits (Fig. 1a), its geological structure and mineralization are of particular interest. Previous studies have focused on the timing of metallogenesis and the formation of hydrothermal deposits in the EKO (Yuan et al., 2003; Feng et al., 2004; Feng et al., 2010a,b; Zhang et al., 2005), and have shown that most of the orogenic gold and porphyry ore deposits formed during the early to middle Triassic. Since the discovery of the Xiarihamu magmatic Ni–Cu sulfide deposit, many additional deposits and areas of mineralization have been discovered in the region (e.g., Binggounan and Shitoukengde), indicating that the EKO is prospective for magmatic Ni–Cu sulfide deposits. However, few studies have examined the metallogenic characteristics and processes of magma evolution of these deposits. It is important to consider whether large magmatic Ni–Cu sulfide deposits can form in an orogenic setting and to investigate the formation mechanism and mineralization process of such deposits, which are poorly understood.

The Xiarihamu Ni–Cu deposit is the first large magmatic Ni–Cu sulfide deposit to be identified in EKO of Qinghai Province, China. The deposit has estimated nickel reserves of 1.07 million tons and associated copper and cobalt metal reserves of 210,000 tons and 40,000 tons, respectively. The average nickel, copper, and cobalt grades are 0.65, 0.13, and 0.025 wt.%, respectively (Li et al., 2012a,b; Sun and Li, 2012; Wang, 2014a). The ore bodies are located in mafic–ultramafic complexes and this setting provides an ideal opportunity to study the relationship between magmatic processes and the formation of Cu–Ni ores, the tectonic setting of magmatic deposits in an orogenic belt, and the nature of the host complex of the Xiarihamu Ni–Cu deposit. The Xiarihamu mafic–ultramafic complexes and associated Ni–Cu ore deposit have not been extensively studied and the few publications that exist are in Chinese (e.g., Li et al., 2012a,b; Ling, 2014; Wang et al., 2014a,b; Jiang et al., 2015). In this paper, new whole-rock geochemistry

and Sr–Nd–Hf and zircon U–Pb isotopic data are presented for the intrusions that host the Xiarihamu Ni–Cu deposit. Furthermore, the processes of formation and the tectonic setting of the intrusions are discussed, providing new information to help resolve the controversy regarding the ore-forming processes and metallogenic conditions of magmatic nickel–copper sulfide deposits.

## 2. Geological background

The Eastern Kunlun Orogen (EKO) belt is located in the western part of the central orogenic belt in mainland China (Fig. 1b), which is bordered by the Qaidam block (QDM) to the north and the Bayan Har-Songanganzi Terrane (BH-SG) to the south. The EKO metallogenic belt trends E–W and is ~1500 km long and 50–200 km wide. In addition, the belt is cut by three closely related, deep E–W regional faults (the North Kunlun, Middle Kunlun, and South Kunlun faults, from north to south) (Huang et al., 1984; Jiang et al., 1992, 2000). Conflicting schemes have been proposed for the division of the tectonic units of the EKO, all of which entail a different tectonic evolution of the region (Xu et al., 1996; Xu, 2006; Xiao and Li, 2000).

Sun et al. (2003), in agreement with previous studies, considered the EKO to be a collage of blocks that accumulated from south to north at the margin of an orogenic belt that experienced multiple stages of orogeny. The North Kunlun, Middle Kunlun, and South Kunlun faults and the southern margin of the A'nyemaqen Block divide the EKO into the North Eastern Kunlun Caledonian back-arc basin belt, the Middle Eastern Kunlun uplifted basement and granitic belt, and the South Eastern Kunlun composite accretion belt (Fig. 1a). Farther south is the A'nyemaqen ophiolite and the North Bayankela orogenic belt. The Middle EKO and North EKO, located north of the Middle Kunlun Fault, have a crystalline basement composed of the Paleoproterozoic Jinshuiko Group. The South EKO is a complex comprising a basaltic oceanic plateau and a continental collage belt.
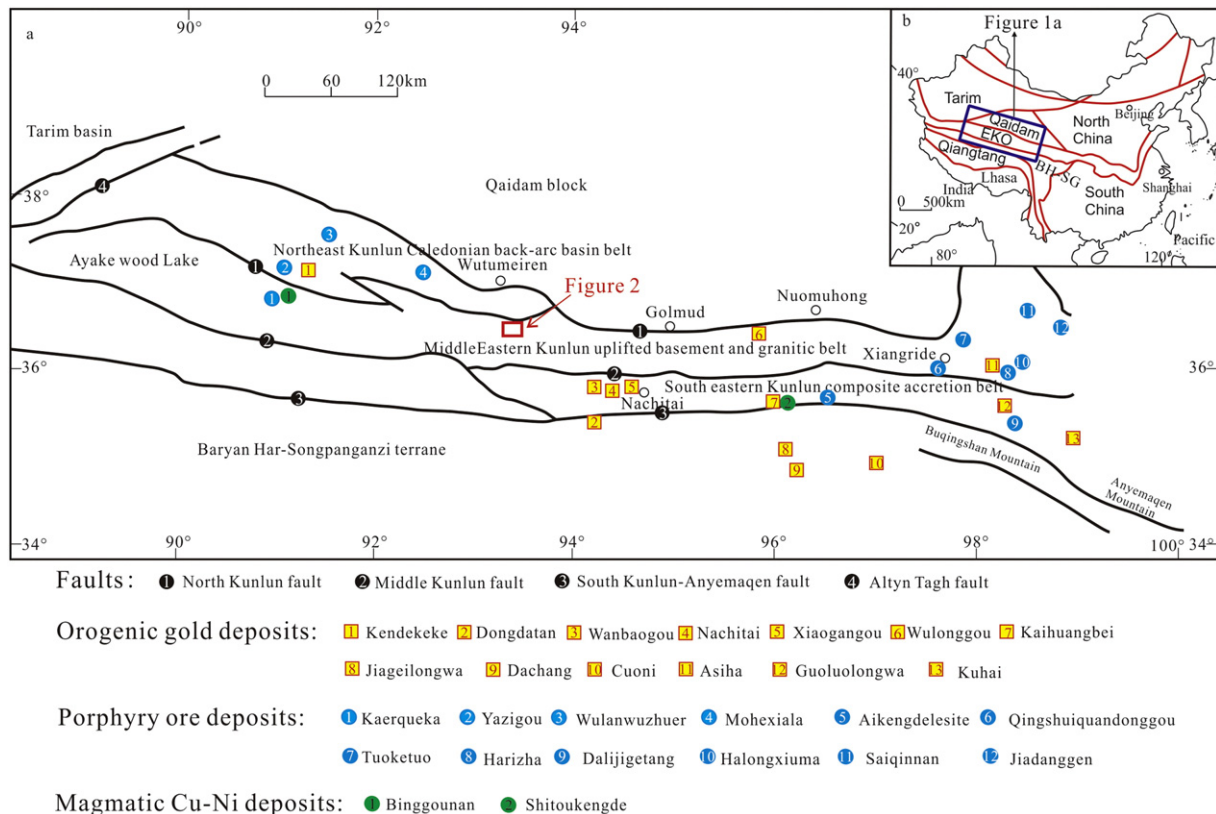


**Fig. 1.** a. Schematic map showing the position of the Eastern Kunlun Orogen(EKO); b. Simplified geological map of the Eastern Kunlun Orogen showing major structures and some important orogenic gold and porphyry ore deposits.

The research area is located in Middle Eastern Kunlun uplifted basement and granitic belt, south of the North Kunlun Fault (Fig. 1a). Exposed strata in the ore district are mainly the Baishahe Formation of the Paleoproterozoic Jinshuiko Group. The main rock types are biotite–plagioclase gneiss, mica monzonite gneiss, amphibolite, and marble. The structures in the ore district are dominated by four sets of faults that strike E–W, N–S, NW–SE, and NE–SW. The largest and oldest structures are those striking E–W throughout the entire deposit, and are transpressional and reverse faults. The NW–SE and NE–SW trending faults formed after the E–W faults and are transpressional reverse faults and dextral strike-slip faults. The N–S faults are the youngest set. The intrusive rocks include diorite, syenogranite, monzonitic granite, and garnet-bearing granitic gneiss, as well as a mafic–ultramafic complex composed of peridotite, pyroxenite, and gabbro in the ore district. The diorite occurs as a small stock and dikes in the southeastern part of the Xiarihamu ore district and yields a zircon $^{206}$Pb/$^{238}$U age of 243 ± 1 Ma (Wang et al., 2014a,b). The syenogranite occurs as a stock in the northern part of the ore district and yields a zircon $^{206}$Pb/$^{238}$U age of 391.1 ± 1.4 Ma (Wang et al., 2013). The Neoproterozoic monzogranite occurs as a small stock in the eastern part of the ore district. The garnet-bearing granitic gneiss crops out in the northwest part of the ore district and yields a zircon $^{206}$Pb/$^{238}$U age of 915–928 Ma (Wang, 2014a). The Ni–Cu ore body and the mineralized body both occur mainly within the mafic–ultramafic complex.

## 3. The Xiarihamu intrusions and Associated Cu–Ni Mineralization

The four mafic–ultramafic complexes in the Xiarihamu region have a ribbon-like distribution trending NW–SE. The exposed area of each intrusion is small, with the largest intrusion having a maximum outcrop area of only 0.7 km². The intrusions range from lopoliths to dikes that were emplaced in Neoproterozoic garnet-bearing granitic gneiss and metamorphic rocks of the Paleoproterozoic Jinshuiko Group (Fig. 2). The Xiarihamu I intrusion is the main host of the Ni–Cu mineralization and yields a zircon $^{206}$Pb/$^{238}$U age of 423 ± 1 Ma (Wang et al., 2014a,b). Economic Ni–Cu sulfide ores have also been discovered in the Xiarihamu II intrusion, where evidence of strong mineralization has been obtained from trench and drill-core samples collected during recent prospecting work. As the two other intrusions do not show any significant mineralization, only intrusions I and II are discussed here.
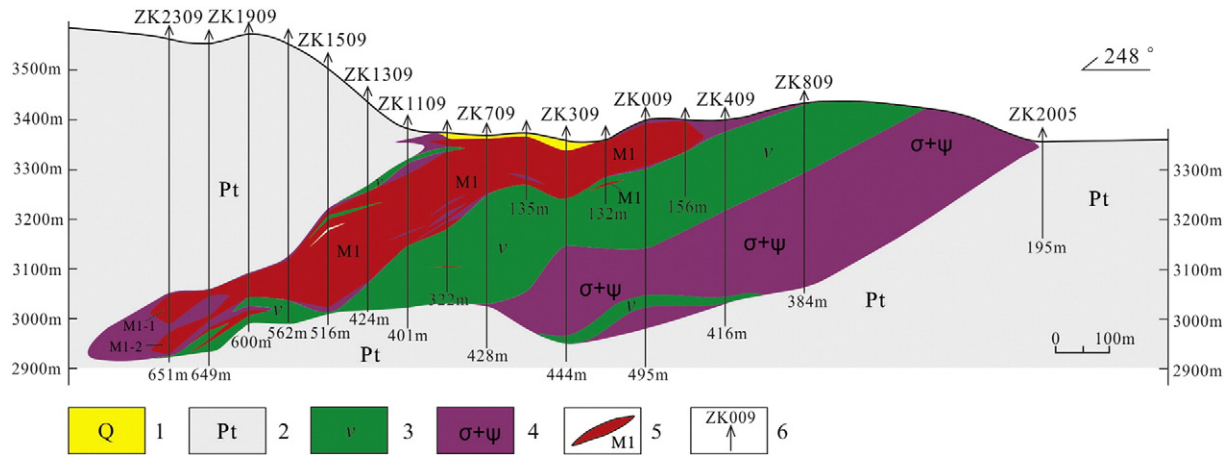
The Xiarihamu I mafic–ultramafic complex is located in the central part of the ore district (Fig. 2), strikes approximately NE–SW, and is elongate. The intrusion is 1.4 km long and 500 m wide and strikes ~060° over an exposed area of ~0.7 km². It is composed mainly of gabbro–norite, ortho-pyroxenite, olivine-pyroxenite, plagio-lherzolite, and orthopyroxene-peridotite. The pyroxenites and peridotite are the main host rocks of the Cu–Ni ores. Star-like sulfide mineralization is also observed in the gabbro–norite, which contains serpentine, talc, and tremolite, and is affected by chloritization and carbonate alteration. The peridotite and pyroxenites are composed of pyrrhotite, pentlandite, and chalcopyrite. Emerald annabergite is observed in outcrops of the olivine- and ortho-pyroxenite.

The Xiarihamu II mafic–ultramafic complex, located in the middle of the ore district (Fig. 2), has intruded gneiss of the Jinshuiko Group and consists of two outcrops. The eastern intrusion strikes ~075°, is 550 m long and 50–240 m wide, and is exposed over ~0.15 km². The intrusion is mainly composed of gabbro with minor pyroxenite. The contact between these two rock types is gradational. The gabbro contains xenoliths of Neoproterozoic monzogranite. Rock samples from a trench excavated at the surface typically contain tremolite and serpentine, display carbonate alteration, and locally contain malachite, annabergite, limonite, pyrrhotite, pentlandite, and chalcopyrite. The western intrusion is 400 m long and 200–350 m wide, and strikes ~090° over an exposed
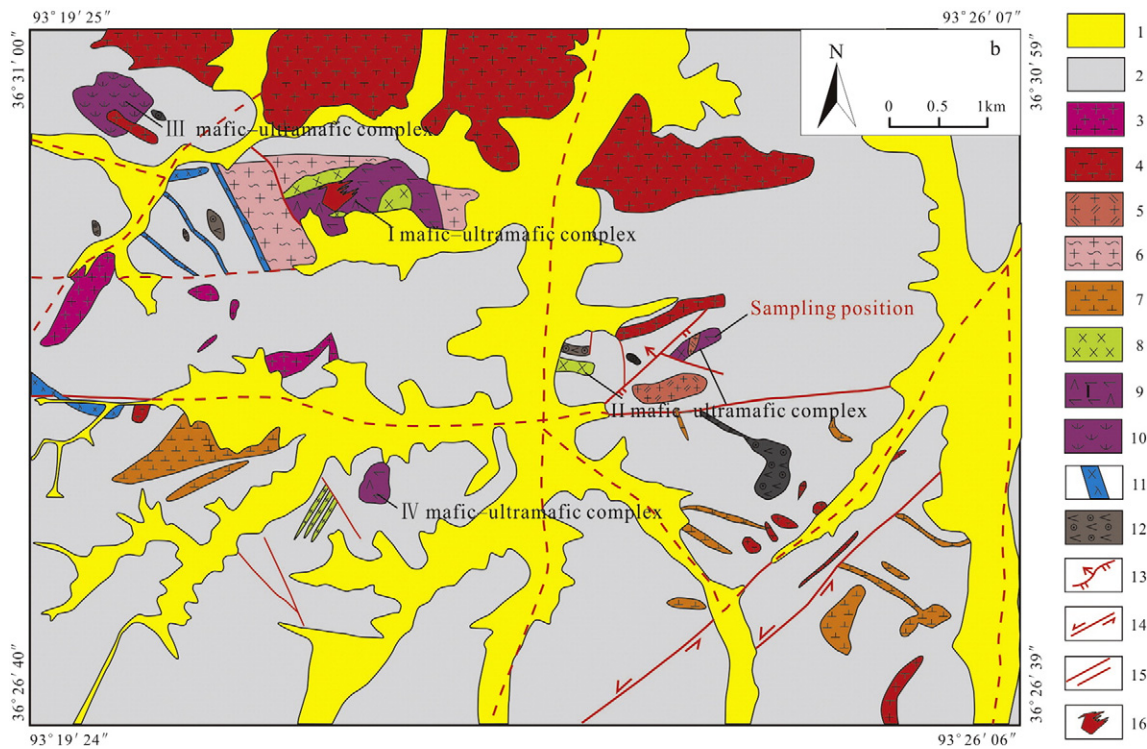


**Fig. 2.** Sketch geological map of the Xiarihamu ore district (modified after Wang et al., 2014b). 1—Quaternary; 2—Proterozoic Jinshuikou rock group; 3—Granite; 4—Middle Devonian fine-grained syenite granite; 5—Neoproterozoic monzogranite; 6—Neoproterozoic granitic gneiss; 7—Lower Trassic fine- to medium-grained diorite; 8—Gabbro; 9—Upper Silurian-Lower Devonian mafic–ultramafic complex; 10—Serpentinite; 11—Diabase; 12—Garnet amphibolite; 13—Reverse fault; 14—Sinistral parallel displacement fault; 15—Nature unknown fault; 16—Nickel ore outcrop.

**Fig. 3.** No. 9 drillings profile map of Xiarihamu I mafic–ultramafic complex. 1—Quaternary; 2—Proterozoic Jinshuikou rock group; 3—Gabbro; 4—Peridotite and pryoxenite; 5—Ore body; 6—Drilling;

area of just ~0.1 km$^2$. The intrusion is composed mainly of gabbro and minor amounts of pyroxenite that is commonly affected by carbonate alteration and ferritization. Massive and star-like pentlandite are also observed in near-surface trench samples.

Twenty economic ore bodies have been discovered within the Xiarihamu I mafic–ultramafic complex. All of the ore bodies are bedded and lenticular, or occur as localized veins of sulfide mineralization. The largest ore body is termed M1 and its genesis appears to have been strongly influenced by the mafic–ultramafic complex. Its strike and dip (~070° and 0–35° to the NW, respectively) are consistent with those of the mafic–ultramafic complex (Fig. 3). The northern part of the ore body tends to be thicker and to have a higher grade than in the southern part, which is split into branches. The form, thickness, and grade of the ore body change significantly along strike from east to west. The ore body in the east (prospecting lines 5–8) is branched,

thin, and has relatively low grades; the ore body in the central region (prospecting lines 7–13) is unbranched and thick; and the ore body in the west (prospecting lines 15–23) is also unbranched but relatively thin. The ore body is generally disseminated and massive. The lower part and base of the ore body are dense and disseminated, while the ore body is locally compact and massive.

Nickel minerals are mainly pentlandite with minor violarite and gersdorffite, copper minerals consist dominantly of chalcopyrite, and iron minerals are mainly pyrrhotite with rare limonite and marcasite. Ore structures include disseminated (Fig. 4a), mottled (Fig. 4b), massive (Fig. 4c), and conglomerations (Fig. 4d). Ore textures include euhedral granular (Fig. 5a), subhedral–anhedral granular (Fig. 5b), sideronitic (Fig. 5c), solid solution separated (Fig. 5d,e) and metasomatic (Fig. 5f).

Samples analyzed in this study were obtained from a trench (TC01, at 93°23′49″E, 36°27′35″N) and the sampling locations are marked
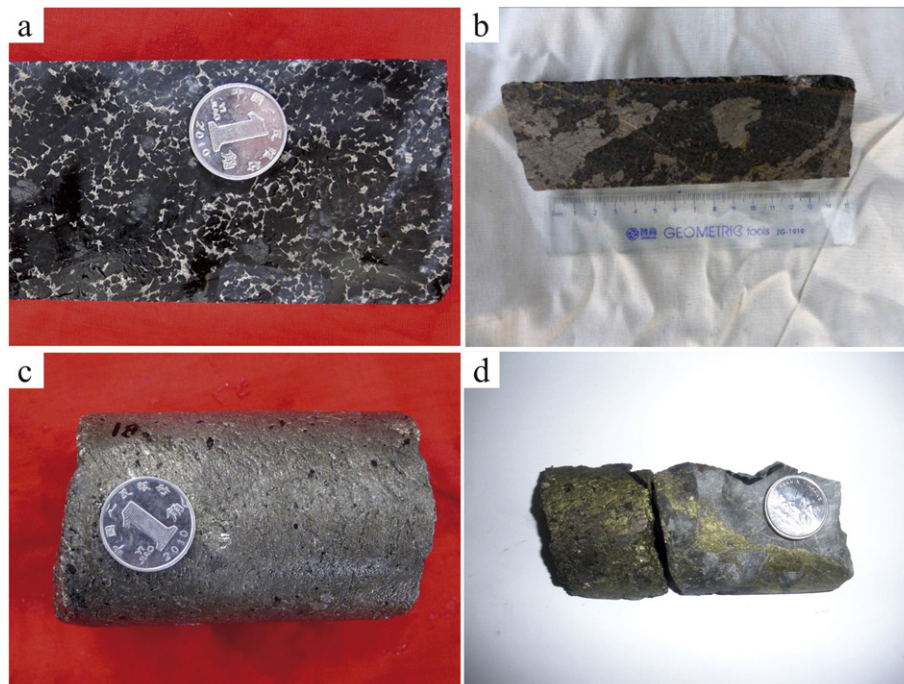


**Fig. 4.** Photographs of ore samples in Xiarihamu mafic–ultramafic complexes.

in Fig. 2. The trench strikes 335° and is 65 m long. The samples are pale gray, altered massive gabbro, with a fine- to medium-grained granoblastic texture. The major minerals are plagioclase (30%–35%) and clinopyroxene (20%–25%) with minor hornblende (Fig. 6a,b). Early-crystallized minerals experienced intensive autometamorphism along fractures due to increasing volatile contents and changes in fluid compositions during the late stages of magmatism, producing serpentine and tremolite. Pyroxene crystals were altered to long, columnar, fibrous tremolite, and serpentine formed along the edges of pyroxene grains.

## 4. Analytical methods

### 4.1. Zircon LA–ICP–MS U–Pb dating and Hf isotopes

Zircons for U–Pb dating were separated in the laboratory at the Regional Geology Survey in Langfang City, Heibei province, China, using standard mineral separation procedures. Zircon grains with clean smooth surfaces that were representative of the different aspect ratios and crystal shapes of the zircon population were mounted in epoxy and then polished to expose crystal cores. Zircons were observed in transmitted light photomicrographs and cathodoluminescence (CL) images to reveal their internal structure.

The zircon U–Pb isotope analysis was under taken at the MLR Key Laboratory of Metallogeny and Mineral Assessment, Institute of Mineral Resources, Chinese Academy of Geosciences, Beijing, China, using a Finnigan Neptune Excel ICP–MS equipped with New Wave UP 213 laser ablation system. A spot diameter of 30 μm was used for the analysis and a Harvard GJ-1 zircon standard was used for external standardization to normalize isotopic fractionation during analysis. The analytical procedures are described by Hou et al. (2009). The data were processed using Isoplot (Ludwig, 2003; Liu et al., 2010a).

The Hf isotope analyses of zircons were performed using laser ablation–multicollector–inductively coupled plasma–mass spectrometry (LA–MC–ICP–MS) at the State Key Laboratory of Geological Processes and Mineral Resources, China University of Geosciences (Wuhan), China. The laser ablation system is a Geolas 2005 (Lambda Physik, Germany), the MC–ICP–MS is a Neptune Plus (Thermo Fisher Scientific, Germany), and the instrument has a beam spot size of 30 μm. The operating conditions and the analytical procedures are described in detail by Hu et al. (2012).

The values of $^{179}Hf/^{177}Hf = 0.7325$ and $^{173}Yb/^{171}Yb = 1.132685$ were used to calculate the quality fractionation factors of Hf and Yb; i.e., βHf and βYb, respectively (Fisher et al., 2014). The ratios of $^{179}Hf/^{177}Hf$ and $^{173}Yb/^{171}Yb$ were used to calculate the quality deviation of Hf (βHf) and Yb (βYb). A value for $^{176}Yb/^{173}Yb$ of 0.79639 was used to deduct $^{176}Yb$ from $^{176}Hf$ isobaric interference. The off-line processing of
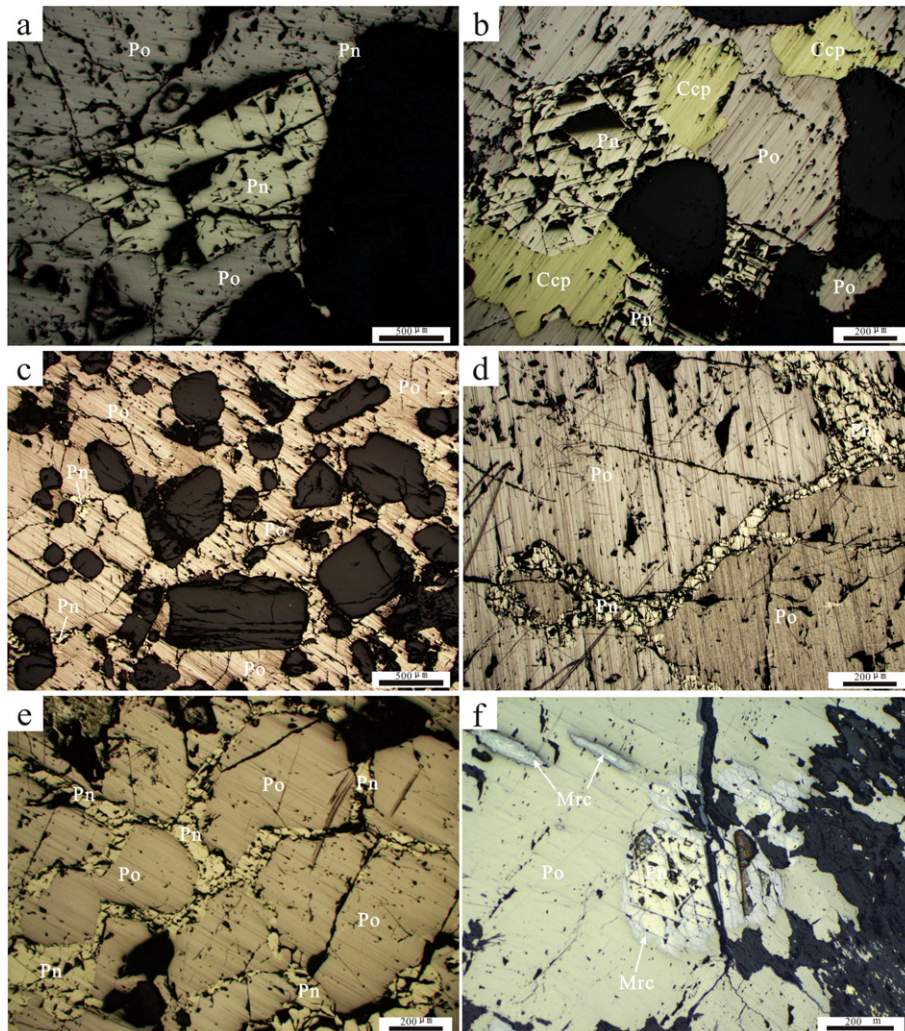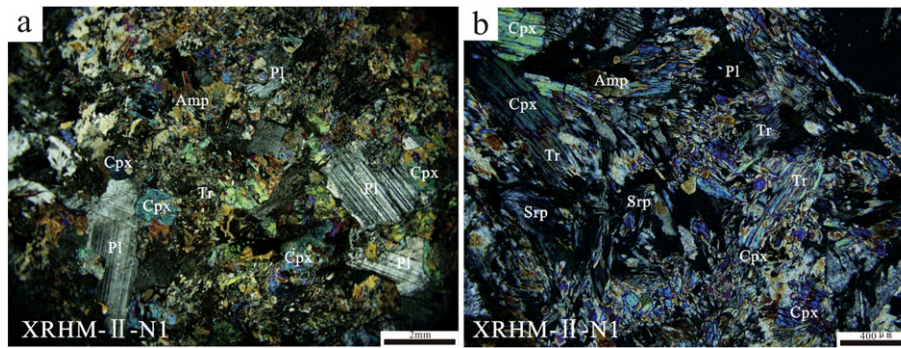


**Fig. 5.** Microphotographs of ore samples in Xiarihamu mafic–ultramafic complexes.

**Fig. 6.** Microphotographs of gabbro sample in Xiarihamu II mafic–ultramafic complex (a—plagioclase polysynthetic twin in gabbro; b—tremolite and talc alteration; Mineral code: Cpx—clinopyroxene, Pl—plagioclase, Amp—amphibole, Tr—tremolite, Srp—serpentine).

analytical data (including the choice of sample and blank signal and isotope fractionation correction quality) was performed using the program ICP–MS Data Cal (Liu et al., 2010b).

### 4.2. Whole-rock major and trace elements

Major and trace element whole-rock analyses were performed at the Beijing Research Institute of Uranium Geology, Beijing, China. Major elements were determined using a Philips X-ray fluorescence spectrometer with detection limits of 0.015 wt.% for $Al_2O_3$, $SiO_2$, MgO, and $Na_2O$; 0.01 wt.% for CaO, $K_2O$, $TiO_2$, and $Fe_2O_3^T$; and 0.005 wt.% for MnO and $P_2O_5$. FeO was determined by the volumetric method with a detection limit of 0.1 wt.%. Trace elements were determined by inductively coupled plasma–mass spectrometry (ICP–MS) using a Finnigan MAT high-resolution ICP–MS (Element I type). Detailed analytical procedures are outlined by Qi et al. (2000).

### 4.3. Whole-rock Sr–Nd isotope analysis

Whole-rock Sr–Nd isotopic analysis was performed at the Institute of Geology and Geophysics, Chinese Academy of Sciences, Beijing, China, using a multi-collector VG354 mass spectrometer in static mode and following the analytical procedures outlined in Chen et al. (2000, 2002a). Approximately 100–150 mg of whole-rock powder was decomposed in a mixture of $HF-HClO_4$ in screw-top Teflon beakers, and Rb, Sr, Sm and Nd were separated by cation exchange columns, following the procedure of Zhang et al. (2001). Rb, Sr, Sm and Nd

concentrations were determined by isotope dilution method, using a mixed $^{87}Rb$–$^{84}Sr$–$^{149}Sm$–$^{150}Nd$ spike solution. Procedural blanks were <200 pg for Sr and <50 pg for Nd. $^{143}Nd/^{144}Nd$ ratios were normalized to $^{146}Nd/^{144}Nd = 0.7219$ and $^{87}Sr/^{86}Sr$ ratios were normalized to $^{86}Sr/^{88}Sr = 0.1194$. Detailed analytical procedures were described in Chen et al. (2000) and Chen et al. (2002b). During the course of this study, standards NBS 607 and BCR-1 gave $^{87}Sr/^{86}Sr$ ratios of 1.20032 ± 28 (2$\sigma$) and $^{143}Nd/^{144}Nd$ ratios of 0.512626 ± 9 (2$\sigma$), respectively. Analytical precision is ~1% for $^{87}Rb/^{86}Sr$ and 0.5% for $^{147}Sm/^{144}Nd$, respectively. Two-stage depleted mantle Nd model ages ($T_{2DM}$) were calculated using the present-day depleted mantle $^{143}Nd/^{144}Nd$ and $^{147}Sm/^{144}Nd$ values of 0.513151 and 0.21357, an average crustal $^{147}Sm/^{144}Nd$ ratio of 0.118 (Jahn and Condie, 1995), and the rock formation ages. The Rb–Sr and Sm–Nd isotopic compositions of samples from the granitic batholiths are presented in Table 4.

## 5. Results

### 5.1. LA–ICP–MS U–Pb zircon dating

Zircons separated from the sample are charcoal gray, mostly wide stubby columnar, and show a clear stripped texture at the edge of zircons. The internal parts of the grains are texturally homogeneous, and there is no oscillatory zoning or inherited cores (Fig. 7). These features are characteristic of zircons from basic intrusions, and are indicative of a magmatic origin.
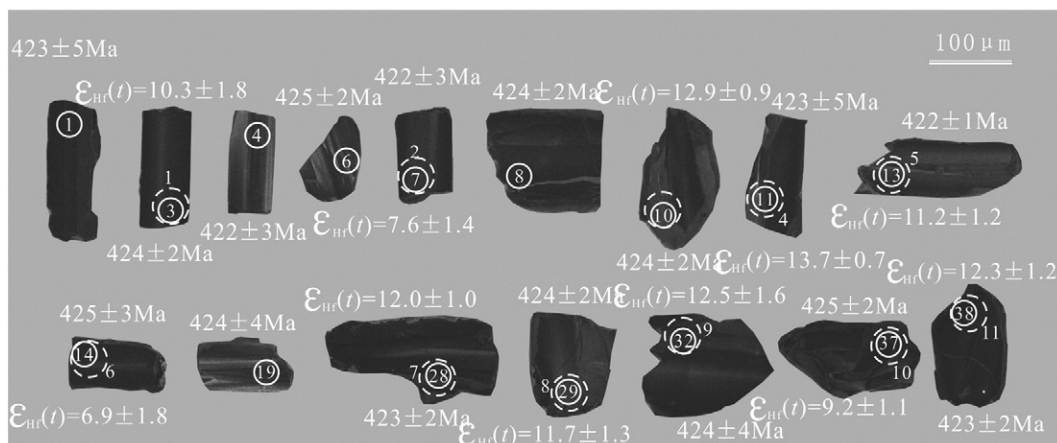


**Fig. 7.** CL images of zircons from gabbro in Xiarihamu II mafic–ultramafic complex.

Thirty-eight analytical spots from 36 zircons are listed in Table 1. The zircon grains have 73–2129 ppm Th, 343–1008 ppm U, and Th/U values of 0.12–2.47. Magmatic zircons typically have Th/U values greater than 0.1 and this is consistent with the interpretation that the zircons in the sample were crystallized from a basic magma. All the analyses are on, or close to, the U–Pb concordia line (Fig. 8). The concordia age obtained from the $^{206}Pb/^{238}U$ analytical data is 424 ± 1 Ma (MSWD = 0.15), which is interpreted as the igneous crystallization age for the Xiarihamu II mafic–ultramafic complex.

### 5.2. Geochemical characteristics

#### 5.2.1. Major elements

Whole-rock major and trace element analyses for samples from the Xiarihamu II mafic–ultramafic complex are listed in Table 2. The samples contain 49.28–52.21 wt.% $SiO_2$ (mean of 50.95 wt.%), 0.49–0.89 wt.% $TiO_2$ (mean of 0.72 wt.%), 10.78–16.91 wt.% $Al_2O_3$ (mean of 14.34 wt.%), 6.95–8.81 wt.% $Fe_2O_3^T$ (mean of 7.84 wt.%), 8.22–17.42 wt.% MgO (mean of 11.54 wt.%), 6.50–10.89 wt.% CaO (mean of 8.87 wt.%), and $Na_2O + K_2O$ contents of 2.04–3.52 wt.% (mean of 2.95 wt.%). The samples have $Mg^\# = 0.70$–0.80 (mean of 0.74) and m/f ($Mg^{2+}/(TFe^{2+} + Mn^{2+})$; Wu, 1963) of 2.32–4.00 (mean 2.87).

The Xiarihamu I mafic–ultramafic complex has similar major element chemistry to the Xiarihamu II mafic–ultramafic complex (Table 2). The gabbro–norite samples from the Xiarihamu I mafic–ultramafic complex contain 50.6–51.39 wt.% $SiO_2$ (mean 50.97 wt.%), 0.37–0.47 wt.% $TiO_2$ (mean 0.4 wt.%), 8.98–13.53 wt.% $Al_2O_3$ (mean 10.57 wt.%), 5.36–8.46 wt.% $Fe_2O_3^T$ (mean 7.41 wt.%), 10.91–16.94 wt.% MgO (mean 15.03 wt.%), 11–14.87 wt.% CaO (mean 12.33 wt.%), and $Na_2O + K_2O$ contents of 1.26–1.95 wt.% (mean 1.56 wt.%).

The two Xiarihamu mafic–ultramafic complexes are rich in MgO and strongly depleted in $SiO_2$, $TiO_2$, and the alkali elements. On a diagram of $FeO^T/MgO$ vs. $SiO_2$ (Fig. 9), the shaded area represents data of the Xiarihamu I mafic–ultramafic complex, and all samples from both complexes plot within the calc-alkaline field, raising the possibility that the two complexes have a common origin.

#### 5.2.2. Trace elements

The trace element abundances of samples from the Xiarihamu II mafic–ultramafic complex are also shown in Table 2. Total rare-earth element contents (ΣREE) are low, ranging from 39.96 to 59.74 ppm. Values for $(La/Yb)_N$ of 2.28–3.04, $(La/Sm)_N$ of 1.67–2.20, and $(Gd/Yb)_N$ of 1.00–1.42 indicate enrichment in light rare earth elements relative to the middle and heavy rare earth elements but only very weak fractionation of the middle and heavy rare earth elements (Fig. 10a). In addition, the samples have δEu values of 0.90–1.09.

On primitive-mantle-normalized spidergrams (Fig. 10b), the samples of gabbro are strongly enriched in LILE (e.g., Rb, Ba, Th, U, and K) and depleted in Nb, Ta, P, and Ti. The shaded area in Fig. 10 represents the REE and trace element patterns of the Xiarihamu I gabbro–norite. The samples from both complexes show similar patterns, further indicating that they have a common source.

**Table 1**
Zircon U-Pb isotopic dating of gabbro samples from the Xiarihamu II mafic–ultramafic complex.

| Analysis | Pb | Th | U | $^{232}Th/^{238}U$ | $^{207}Pb/^{206}Pb$ | | $^{207}Pb/^{235}U$ | | $^{206}Pb/^{238}U$ | | $^{207}Pb/^{206}Pb$ | | $^{207}Pb/^{235}U$ | | $^{206}Pb/^{238}U$ | | $^{208}Pb/^{232}Th$ | |
|---|---|---|---|---|---|---|---|---|---|---|---|---|---|---|---|---|---|---|
| | ppm | ppm | ppm | | Ratio | 1σ | Ratio | 1σ | Ratio | 1σ | Age(Ma) | 1σ | Age(Ma) | 1σ | Age(Ma) | 1σ | Age(Ma) | 1σ |
| XRHM- II-N1-1 | 1665 | 1014 | 701 | 1.45 | 0.05583 | 0.00031 | 0.5226 | 0.00781 | 0.06786 | 0.00083 | 456 | 13 | 427 | 5 | 423 | 5 | 559 | 40 |
| XRHM- II-N1-2 | 1209 | 771 | 674 | 1.14 | 0.05555 | 0.00017 | 0.51994 | 0.00488 | 0.06787 | 0.0006 | 435 | 7 | 425 | 3 | 423 | 4 | 559 | 36 |
| XRHM- II-N1-3 | 1356 | 839 | 783 | 1.07 | 0.05548 | 0.00015 | 0.51952 | 0.00277 | 0.0679 | 0.00032 | 432 | 3 | 425 | 2 | 424 | 2 | 588 | 37 |
| XRHM- II-N1-4 | 2204 | 1434 | 813 | 1.76 | 0.05574 | 0.00031 | 0.5203 | 0.0051 | 0.06769 | 0.00052 | 443 | 13 | 425 | 3 | 422 | 3 | 580 | 38 |
| XRHM- II-N1-5 | 1012 | 646 | 802 | 0.81 | 0.05587 | 0.0003 | 0.52276 | 0.00641 | 0.06785 | 0.00074 | 456 | 11 | 427 | 4 | 423 | 4 | 611 | 44 |
| XRHM- II-N1-6 | 1224 | 879 | 678 | 1.3 | 0.05517 | 0.00014 | 0.51829 | 0.0032 | 0.06813 | 0.00039 | 420 | 10 | 424 | 2 | 425 | 2 | 561 | 43 |
| XRHM- II-N1-7 | 1110 | 798 | 898 | 0.89 | 0.05529 | 0.0002 | 0.51581 | 0.00411 | 0.06766 | 0.0005 | 433 | 7 | 422 | 3 | 422 | 3 | 567 | 47 |
| XRHM- II-N1-8 | 2216 | 1716 | 975 | 1.76 | 0.05569 | 0.00016 | 0.52175 | 0.00314 | 0.06795 | 0.00037 | 439 | 10 | 426 | 2 | 424 | 2 | 468 | 41 |
| XRHM- II-N1-9 | 825 | 649 | 534 | 1.22 | 0.05552 | 0.00031 | 0.52093 | 0.00565 | 0.0681 | 0.00076 | 432 | 18 | 426 | 4 | 425 | 5 | 429 | 37 |
| XRHM- II-N1-10 | 811 | 597 | 590 | 1.01 | 0.05589 | 0.00031 | 0.52416 | 0.00444 | 0.068 | 0.00041 | 456 | 13 | 428 | 3 | 424 | 2 | 319 | 39 |
| XRHM- II-N1-11 | 1692 | 1273 | 866 | 1.47 | 0.05523 | 0.00032 | 0.51709 | 0.00657 | 0.0679 | 0.00078 | 420 | 13 | 423 | 4 | 423 | 5 | 248 | 44 |
| XRHM- II-N1-12 | 2216 | 1775 | 968 | 1.83 | 0.05602 | 0.00025 | 0.52465 | 0.00298 | 0.06799 | 0.00031 | 454 | 11 | 428 | 2 | 424 | 2 | 244 | 38 |
| XRHM- II-N1-13 | 1545 | 1208 | 1008 | 1.2 | 0.05629 | 0.00023 | 0.52492 | 0.00288 | 0.06768 | 0.00024 | 465 | 9 | 428 | 2 | 422 | 1 | 267 | 35 |
| XRHM- II-N1-14 | 857 | 753 | 641 | 1.18 | 0.05535 | 0.00045 | 0.51993 | 0.00642 | 0.06817 | 0.00044 | 428 | 23 | 425 | 4 | 425 | 3 | 254 | 29 |
| XRHM- II-N1-15 | 2604 | 2128 | 863 | 2.47 | 0.05542 | 0.00045 | 0.51741 | 0.00382 | 0.06777 | 0.0004 | 428 | 23 | 423 | 3 | 423 | 2 | 314 | 29 |
| XRHM- II-N1-16 | 111 | 73 | 599 | 0.12 | 0.05479 | 0.00017 | 0.51548 | 0.00267 | 0.06829 | 0.00029 | 467 | 6 | 422 | 2 | 426 | 2 | 362 | 33 |
| XRHM- II-N1-17 | 534 | 456 | 397 | 1.15 | 0.05609 | 0.00038 | 0.52451 | 0.00493 | 0.06797 | 0.00047 | 457 | 15 | 428 | 3 | 423 | 3 | 348 | 30 |
| XRHM- II-N1-18 | 2735 | 2087 | 982 | 2.13 | 0.05634 | 0.00034 | 0.527 | 0.00647 | 0.06787 | 0.00085 | 465 | 13 | 430 | 4 | 423 | 5 | 434 | 39 |
| XRHM- II-N1-19 | 2269 | 1788 | 834 | 2.14 | 0.05543 | 0.00036 | 0.51965 | 0.00524 | 0.06801 | 0.00061 | 428 | 13 | 425 | 4 | 424 | 4 | 452 | 35 |
| XRHM- II-N1-20 | 807 | 664 | 575 | 1.15 | 0.05498 | 0.00026 | 0.51708 | 0.00494 | 0.06821 | 0.00036 | 413 | −23 | 423 | 3 | 425 | 2 | 434 | 32 |
| XRHM- II-N1-21 | 477 | 363 | 343 | 1.06 | 0.05503 | 0.00023 | 0.51561 | 0.00426 | 0.06805 | 0.0006 | 413 | 14 | 422 | 3 | 424 | 4 | 482 | 36 |
| XRHM- II-N1-22 | 1561 | 1142 | 835 | 1.37 | 0.05579 | 0.00026 | 0.52319 | 0.00471 | 0.06806 | 0.00062 | 443 | 9 | 427 | 3 | 424 | 4 | 517 | 40 |
| XRHM- II-N1-23 | 389 | 301 | 397 | 0.76 | 0.05555 | 0.00069 | 0.51898 | 0.00619 | 0.06784 | 0.00089 | 435 | 28 | 424 | 4 | 423 | 5 | 495 | 45 |
| XRHM- II-N1-24 | 1248 | 820 | 697 | 1.18 | 0.05593 | 0.00018 | 0.52373 | 0.00386 | 0.06791 | 0.00043 | 450 | 7 | 428 | 3 | 424 | 3 | 602 | 58 |
| XRHM- II-N1-25 | 608 | 408 | 547 | 0.75 | 0.05511 | 0.00028 | 0.51837 | 0.00646 | 0.06826 | 0.00087 | 417 | 11 | 424 | 4 | 426 | 5 | 588 | 61 |
| XRHM- II-N1-26 | 1308 | 933 | 790 | 1.18 | 0.0559 | 0.00018 | 0.52266 | 0.0041 | 0.06788 | 0.00054 | 450 | 7 | 427 | 3 | 423 | 3 | 555 | 50 |
| XRHM- II-N1-27 | 782 | 591 | 615 | 0.96 | 0.0553 | 0.00023 | 0.51841 | 0.0028 | 0.06799 | 0.00026 | 433 | 9 | 424 | 2 | 424 | 2 | 512 | 43 |
| XRHM- II-N1-28 | 923 | 724 | 472 | 1.53 | 0.0554 | 0.00039 | 0.518 | 0.00395 | 0.06783 | 0.00031 | 428 | 15 | 424 | 3 | 423 | 2 | 460 | 33 |
| XRHM- II-N1-29 | 497 | 394 | 448 | 0.88 | 0.05562 | 0.00018 | 0.52101 | 0.00274 | 0.06796 | 0.00032 | 439 | 6 | 426 | 2 | 424 | 2 | 420 | 35 |
| XRHM- II-N1-30 | 635 | 509 | 462 | 1.1 | 0.05537 | 0.00017 | 0.51876 | 0.00261 | 0.06795 | 0.00028 | 428 | 7 | 424 | 2 | 424 | 2 | 411 | 30 |
| XRHM- II-N1-31 | 652 | 510 | 407 | 1.25 | 0.05584 | 0.00047 | 0.52277 | 0.0051 | 0.06789 | 0.00029 | 456 | 19 | 427 | 3 | 423 | 2 | 417 | 27 |
| XRHM- II-N1-32 | 547 | 414 | 439 | 0.94 | 0.05589 | 0.00025 | 0.52335 | 0.00482 | 0.06794 | 0.00062 | 428 | 9 | 427 | 3 | 424 | 4 | 425 | 27 |
| XRHM- II-N1-33 | 716 | 520 | 465 | 1.12 | 0.05535 | 0.00022 | 0.51922 | 0.00348 | 0.06805 | 0.00039 | 428 | 9 | 425 | 2 | 424 | 2 | 447 | 30 |
| XRHM- II-N1-34 | 724 | 476 | 544 | 0.88 | 0.05535 | 0.0002 | 0.51715 | 0.00255 | 0.06785 | 0.00035 | 428 | 9 | 423 | 2 | 423 | 2 | 481 | 34 |
| XRHM- II-N1-35 | 1046 | 745 | 630 | 1.18 | 0.05552 | 0.00021 | 0.51971 | 0.00274 | 0.0679 | 0.00029 | 432 | 5 | 425 | 2 | 424 | 2 | 435 | 27 |
| XRHM- II-N1-36 | 934 | 624 | 672 | 0.93 | 0.05537 | 0.00015 | 0.51927 | 0.00329 | 0.06804 | 0.00042 | 428 | 7 | 425 | 2 | 424 | 3 | 459 | 30 |
| XRHM- II-N1-37 | 888 | 603 | 643 | 0.94 | 0.05595 | 0.00019 | 0.52539 | 0.00308 | 0.06811 | 0.00036 | 450 | 7 | 429 | 2 | 425 | 2 | 449 | 32 |
| XRHM- II-N1-38 | 785 | 495 | 604 | 0.82 | 0.05556 | 0.00016 | 0.52028 | 0.00362 | 0.0679 | 0.00041 | 435 | 7 | 425 | 2 | 423 | 2 | 475 | 36 |
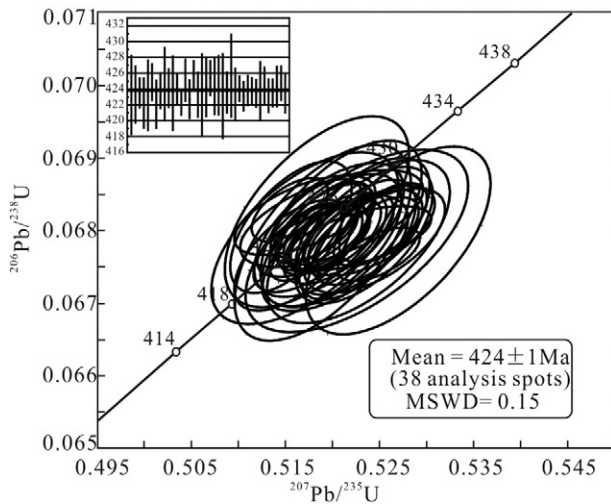
**Fig. 8.** Zircons U–Pb concordia diagram for gabbro in Xiarihamu II mafic–ultramafic complex.

### 5.3. Hf isotopes of zircon

Eleven analytical spots on zircon grains from the Xiarihamu II gabbro samples were analyzed for their Hf isotopic compositions. The $^{176}Yb/^{177}Hf$ values of the spots range from 0.043162 to 0.087326 and their $^{176}Lu/^{177}Hf$ values are between 0.001092 and 0.002359 (Table 3). Individual spots generally yield $^{176}Lu/^{177}Hf$ values slightly greater than 0.002. The $^{176}Hf/^{177}Hf$ values of the 11 analytical spot are between 0.282721 and 0.282912, corresponding to $\varepsilon_{Hf}(t)$ values of 6.9–13.7, with a weighted mean of 11.7. The zircon model ages ($t_{DM1}$) range from 775 to 497 Ma, with a mean of 608 Ma.

Thirteen spots on zircon grains from the Xiarihamu I gabbro–norite samples were analyzed for Hf isotopic compositions. The $^{176}Yb/^{177}Hf$ values range from 0.023908 to 0.085542 and the $^{176}Lu/^{177}Hf$ values from 0.000625 to 0.001965 (Table 3). All spots generally yield $^{176}Lu/^{177}Hf$ values of less than 0.002. The $^{176}Hf/^{177}Hf$ values are between 0.282628 and 0.282833, corresponding to $\varepsilon Hf_{(t)}$ values of 4.0–10.9, with a weighted mean of 6.5. The zircon model ages ($t_{DM1}$) range from 610 to 875 Ma, with a mean of 788 Ma.

Both of the Xiarihamu mafic–ultramafic complexes have positive $\varepsilon Hf_{(t)}$ values and zircon Hf model ages ($t_{DM1}$) that are considerably older than their crystallization ages. The shaded area in Fig. 11 represents data of the Xiarihamu I mafic–ultramafic complex, and Hf isotopic data from both complexes plot between the Hf isotopic evolution lines of chondrite and depleted mantle, closer to the depleted mantle line (Fig. 11).

### 5.4. Whole-rock Sr–Nd isotopes

The whole-rock Sr–Nd isotopic data of the studied samples are presented in Table 4. The samples of gabbro from the Xiarihamu II complex have $\varepsilon_{Nd}(t)$ values of −2.1 to −0.7 (at t = 424 Ma) and $(^{87}Sr/^{86}Sr)_i =$ 0.708200–0.708614 (mean 0.708415). The samples from the Xiarihamu I complex have $\varepsilon_{Nd}(t)$ values of −0.2 to −3.1 (at t = 422 Ma) and $(^{87}Sr/^{86}Sr)_i = $ 0.703105–0.710932 (mean 0.705811). Therefore, the two Xiarihamu mafic–ultramafic complexes have similar Sr and Nd isotopic compositions. Both of the complexes have relatively small negative $\varepsilon_{Nd}(t)$ values and $(^{87}Sr/^{86}Sr)_i$ values that are higher than those of MORB (Saunders et al., 1988). On a diagram of $\varepsilon_{Nd}(t)$ vs. $(^{87}Sr/^{86}Sr)_i$ (Fig. 12a), the samples from the Xiarihamu I complex are dispersed and plot in the third and fourth quadrants, while the

samples from the Xiarihamu II complex are clustered and all plot in the fourth quadrant. Therefore, the Sr and Nd isotopes of both complexes show evidence for evolution from an EMII end-member composition.

## 6. Discussion

### 6.1. Sources

The major and trace element characteristics, and Sr, Nd, and Hf isotopic compositions of the two Xiarihamu mafic–ultramafic complexes suggest that they were derived from a common source. The Hf isotopic compositions of zircons from the two complexes all have positive $\varepsilon Hf_{(t)}$ values that are close to that of depleted mantle (Fig. 11), indicating the complexes formed by partial melting of depleted mantle. However, the zircons have Hf model ages ($t_{DM1}$) that are considerably older than their crystallization ages. The Hf model ages of zircons may reflect the time at which they separated from depleted mantle, if the parental magma of the zircons came directly from unmodified depleted mantle. In such a case, the crystallization ages of the zircons should be roughly the same as the Hf model ages of the zircons (Wu et al., 2004, 2007). The fact that the Hf model ages are considerably older than the igneous crystallization age for the Xiarihamu mafic–ultramafic complex implies that the source of the magma had experienced some enrichment.

It is inevitable that mantle-derived magma will experience assimilation–contamination during ascent, and such processes are evident within the Xiarihamu intrusion as it contains numerous xenoliths of Neoproterozoic monzogranite. The samples of gabbro show strong enrichment in LILE (e.g., Rb, Ba, Th, U, and K) and depletion in HFSE (e.g., Nb, Ta, and Ti) and the chondrite-normalized REE patterns of samples from the Xiarihamu mafic–ultramafic complexes are different from those of N-MORB sourced from asthenospheric mantle (Fig. 10a). On a diagram of $\varepsilon_{Nd}(t)$ vs. $(^{87}Sr/^{86}Sr)_i$ (Fig. 12), samples from the complexes define a trend toward the EMII end member and may form an array between the DMM and EMII end members. The EMI end member appears to be unimportant. The isotopic composition of EMII mantle is similar to that of terrigenous sediment and is closely related to subducted and recycled crust, whereas the EMI mantle component is considered to originate from lithospheric mantle under the continents (Hart, 1988; McKenzie, 1989; Menzies, 1990). Therefore, we infer that the parental magma of the Xiarihamu mafic–ultramafic complexes originated from asthenospheric mantle that subsequently became enriched in EMII during ascent.

The ratios of elements with the same or very similar distribution coefficients are unaffected by fractional crystallization and partial melting (Campbell and Griffiths, 1993; Baker et al., 1997; MacDonald et al., 2001). Therefore, the covariant relationships among these elements and their ratios (e.g., Th/Yb, Zr/Yb, Nb/Ta, Ce/Pb, Ta/Yb, $K_2O/P_2O_5$) are sensitive to contamination, and can effectively verify whether assimilation and contamination occurred, and indicate the degree of contamination. Fig. 13a and b shows a positive correlation between Zr and Th, and between Th/Yb and Nb/La. The values of Nb/U and Ce/Pb do not change during partial melting and magmatic differentiation; consequently, their distribution coefficients remain constant and are indicative of their origin. MORB and OIB have high, uniform Nb/U ratios of 47 ± 10 (Hofmann, 1988). In contrast, the Nb/U ratio of the Xiarihamu II intrusion is 2.89–3.60 and that of the Xiarihamu I intrusion is 2.65–4.38, which are both similar to the mean values of continental crust (~9.7; Campbell, 2002). The average Ce/Pb ratio of the mantle is 25 ± 5, whereas that of continental crust is <15 (Furman et al., 2004). The Ce/Pb ratios of the Xiarihamu II intrusion range from 1.1 to 3.98 with a mean of 3.21, which are different to mantle values but relatively similar to continental crust values, suggesting significant crustal contamination.

**Table 2**
Contents of major elements (wt.%) and trace elements(×10–6) of samples.

| Samples | XRHM-II-Y1 | XRHM-II-Y2 | XRHM-II-Y3 | XRHM-II-Y4 | XRHM-II-Y5 | XRHM-II-Y6 | XRHM-II-Y7 | XRHM-II-Y8 | XRHM-II-Y9 | XRHM-I-Y1* | XRHM-I-Y2* | XRHM-I-Y3* | XRHM-I-Y4* | XRHM-I-Y5* | XRHM-I-Y6* |
|---|---|---|---|---|---|---|---|---|---|---|---|---|---|---|---|
| $SiO_2$ | 50.74 | 51.96 | 52.21 | 50.92 | 51.05 | 50.39 | 49.28 | 50.97 | 51.05 | 51.19 | 51.39 | 50.99 | 51.05 | 50.62 | 50.60 |
| $TiO_2$ | 0.49 | 0.62 | 0.89 | 0.80 | 0.67 | 0.72 | 0.73 | 0.77 | 0.80 | 0.37 | 0.40 | 0.36 | 0.40 | 0.42 | 0.47 |
| $Al_2O_3$ | 10.78 | 13.06 | 13.24 | 14.70 | 14.56 | 14.74 | 14.83 | 16.21 | 16.91 | 9.91 | 8.98 | 9.63 | 9.74 | 13.53 | 11.60 |
| $TFe_2O_3$ | 8.53 | 7.99 | 8.81 | 8.03 | 7.36 | 7.58 | 7.90 | 7.37 | 6.95 | 8.17 | 8.40 | 8.46 | 7.80 | 5.36 | 6.28 |
| MnO | 0.16 | 0.15 | 0.17 | 0.14 | 0.13 | 0.12 | 0.13 | 0.12 | 0.11 | 0.14 | 0.14 | 0.14 | 0.13 | 0.12 | 0.14 |
| MgO | 17.42 | 13.00 | 12.58 | 9.99 | 11.68 | 10.96 | 11.21 | 8.76 | 8.22 | 16.54 | 16.94 | 16.72 | 16.21 | 10.91 | 12.88 |
| CaO | 6.50 | 8.18 | 7.28 | 10.89 | 9.13 | 8.91 | 8.49 | 10.25 | 10.21 | 11.04 | 11.94 | 11.00 | 11.81 | 14.87 | 13.30 |
| $Na_2O$ | 1.55 | 2.03 | 2.29 | 2.34 | 2.38 | 2.54 | 2.56 | 2.61 | 2.78 | 1.18 | 1.09 | 1.16 | 1.22 | 1.67 | 1.33 |
| $K_2O$ | 0.49 | 0.66 | 0.69 | 0.54 | 0.36 | 0.87 | 0.39 | 0.74 | 0.74 | 0.21 | 0.17 | 0.18 | 0.29 | 0.28 | 0.58 |
| $P_2O_5$ | 0.05 | 0.06 | 0.08 | 0.07 | 0.08 | 0.09 | 0.08 | 0.08 | 0.09 | 0.02 | 0.02 | 0.02 | 0.02 | 0.02 | 0.02 |
| LOI | 3.29 | 2.24 | 1.75 | 1.64 | 2.62 | 2.82 | 3.05 | 1.66 | 1.63 | 1.04 | 0.40 | 0.79 | 1.00 | 2.16 | 2.78 |
| Total | 100.00 | 99.96 | 99.99 | 100.06 | 100.02 | 99.86 | 98.75 | 99.65 | 99.58 | 99.81 | 99.87 | 99.45 | 99.67 | 99.96 | 99.98 |
| $K_2O + Na_2O$ | 2.04 | 2.69 | 2.98 | 2.88 | 2.74 | 3.41 | 2.95 | 3.35 | 3.52 | 1.39 | 1.26 | 1.34 | 1.51 | 1.95 | 1.91 |
| Mg#Mg#Mg# | 80.00 | 76.00 | 74.00 | 71.00 | 76.00 | 74.00 | 74.00 | 70.00 | 70.00 | 80 | 80 | 80 | 81 | 80 | 80 |
| m/f | 4.00 | 3.19 | 2.80 | 2.44 | 3.11 | 2.84 | 2.79 | 2.33 | 2.32 | 3.97 | 3.96 | 3.88 | 4.08 | 3.97 | 4.01 |
| La | 6.11 | 7.70 | 9.88 | 7.80 | 7.40 | 8.70 | 8.10 | 6.50 | 7.40 | 3.00 | 2.70 | 2.80 | 3.00 | 4.15 | 4.59 |
| Ce | 12.10 | 15.90 | 19.70 | 18.80 | 16.40 | 19.90 | 18.30 | 15.60 | 17.20 | 7.40 | 6.80 | 6.80 | 7.10 | 9.08 | 11.00 |
| Pr | 1.60 | 2.20 | 2.57 | 2.46 | 2.03 | 2.65 | 2.27 | 2.04 | 2.19 | 1.16 | 1.13 | 1.06 | 1.13 | 1.42 | 1.77 |
| Nd | 7.91 | 10.50 | 11.60 | 11.10 | 9.10 | 10.80 | 9.90 | 9.30 | 9.50 | 4.90 | 4.90 | 4.60 | 5.00 | 7.45 | 9.18 |
| Sm | 1.92 | 2.54 | 2.82 | 2.88 | 2.30 | 2.98 | 2.52 | 2.45 | 2.46 | 1.37 | 1.47 | 1.34 | 1.51 | 2.16 | 2.64 |
| Eu | 0.69 | 0.86 | 0.91 | 1.05 | 0.86 | 0.92 | 0.92 | 1.01 | 1.02 | 0.59 | 0.58 | 0.55 | 0.56 | 0.77 | 0.90 |
| Gd | 2.24 | 2.89 | 2.77 | 3.85 | 2.91 | 3.21 | 3.21 | 3.26 | 3.22 | 2.01 | 2.15 | 1.91 | 2.06 | 2.34 | 2.85 |
| Tb | 0.47 | 0.59 | 0.59 | 0.63 | 0.46 | 0.53 | 0.51 | 0.54 | 0.52 | 0.35 | 0.35 | 0.32 | 0.33 | 0.53 | 0.57 |
| Dy | 2.58 | 3.48 | 3.43 | 3.83 | 2.87 | 3.22 | 3.05 | 3.25 | 3.15 | 1.94 | 2.05 | 1.82 | 1.94 | 2.63 | 3.28 |
| Ho | 0.48 | 0.65 | 0.67 | 0.76 | 0.56 | 0.66 | 0.62 | 0.65 | 0.62 | 0.40 | 0.44 | 0.39 | 0.41 | 0.52 | 0.64 |
| Er | 1.54 | 1.94 | 1.90 | 2.33 | 1.74 | 1.95 | 1.87 | 2.02 | 1.87 | 1.28 | 1.36 | 1.25 | 1.30 | 1.37 | 1.83 |
| Tm | 0.29 | 0.35 | 0.36 | 0.32 | 0.25 | 0.28 | 0.28 | 0.29 | 0.27 | 0.18 | 0.20 | 0.17 | 0.18 | 0.24 | 0.31 |
| Yb | 1.79 | 2.14 | 2.23 | 2.21 | 1.75 | 1.93 | 1.89 | 1.92 | 1.83 | 1.02 | 1.14 | 1.02 | 1.04 | 1.35 | 1.82 |
| Lu | 0.23 | 0.29 | 0.31 | 0.32 | 0.25 | 0.28 | 0.26 | 0.28 | 0.26 | 0.16 | 0.16 | 0.16 | 0.16 | 0.19 | 0.23 |
| ΣREE | 39.96 | 52.04 | 59.74 | 58.34 | 48.88 | 58.01 | 53.70 | 49.11 | 51.51 | 25.76 | 25.43 | 24.19 | 25.72 | 34.19 | 41.61 |
| (La/Sm)N(La/Sm)N | 2.00 | 1.91 | 2.20 | 1.70 | 2.02 | 1.84 | 2.02 | 1.67 | 1.89 | 1.38 | 1.16 | 1.31 | 1.25 | 1.21 | 1.09 |
| (La/Yb)N(La/Yb)N | 2.30 | 2.43 | 2.99 | 2.38 | 2.85 | 3.04 | 2.89 | 2.28 | 2.73 | 1.98 | 1.60 | 1.85 | 1.94 | 2.07 | 1.70 |
| (Gd/Yb)N(Gd/Yb)N | 1.01 | 1.09 | 1.00 | 1.41 | 1.34 | 1.34 | 1.37 | 1.37 | 1.42 | 1.59 | 1.52 | 1.51 | 1.60 | 1.40 | 1.26 |
| δEu | 1.00 | 0.96 | 0.98 | 0.95 | 1.00 | 0.90 | 0.98 | 1.08 | 1.09 | 1.07 | 0.98 | 1.04 | 0.96 | 1.03 | 0.99 |
| V | 166.00 | 161.00 | 153.00 | 208.00 | 160.00 | 178.00 | 172.00 | 168.00 | 162.00 | 246.00 | 252.00 | 245.00 | 240.00 | 185.00 | 245.00 |
| Cr | 1793.00 | 1049.00 | 894.00 | 440.00 | 720.00 | 580.00 | 660.00 | 250.00 | 230.00 | 1240.00 | 1380.00 | 1260.00 | 1320.00 | 375.00 | 619.00 |
| Co | 62.00 | 49.00 | 49.00 | 44.00 | 45.00 | 45.00 | 48.00 | 39.00 | 38.00 | 65.00 | 68.00 | 72.00 | 62.00 | 42.00 | 55.00 |
| Ni | 326.00 | 201.00 | 190.00 | 150.00 | 194.00 | 186.00 | 193.00 | 111.00 | 99.00 | 251.00 | 297.00 | 305.00 | 269.00 | 345.00 | 184.00 |
| Cu | 28.00 | 39.00 | 44.00 | 59.00 | 29.00 | 36.00 | 30.00 | 40.00 | 55.00 | | | | | | |
| Zn | 66.00 | 72.00 | 68.00 | 66.00 | 65.00 | 58.00 | 61.00 | 59.00 | 59.00 | | | | | | |
| Ga | 9.82 | 11.60 | 12.50 | 14.90 | 14.00 | 15.50 | 15.10 | 15.30 | 16.10 | | | | | | |
| Rb | 39.50 | 34.50 | 33.60 | 31.20 | 20.20 | 54.50 | 20.00 | 46.50 | 48.20 | 9.00 | 7.40 | 7.60 | 17.30 | 12.00 | 52.10 |
| Ba | 119.00 | 161.00 | 169.00 | 154.50 | 94.00 | 176.50 | 92.90 | 186.00 | 200.00 | 49.60 | 41.50 | 44.70 | 53.20 | 73.10 | 110.00 |
| Sr | 122.00 | 190.00 | 197.00 | 231.00 | 208.00 | 260.00 | 223.00 | 271.00 | 290.00 | 173.50 | 140.50 | 166.50 | 165.00 | 272.00 | 287.00 |
| Y | 13.10 | 17.80 | 17.60 | 21.40 | 16.20 | 18.80 | 17.50 | 18.60 | 17.80 | 9.60 | 10.40 | 9.60 | 10.10 | 13.30 | 16.50 |
| Nb | 1.48 | 2.14 | 2.95 | 2.50 | 2.20 | 2.90 | 2.60 | 2.60 | 3.10 | 0.40 | 0.40 | 0.70 | 0.60 | 0.60 | 0.61 |
| Ta | 0.13 | 0.19 | 0.24 | 0.20 | 0.20 | 0.20 | 0.20 | 0.20 | 0.20 | 0.1 | 0.1 | 0.10 | 0.1 | 0.05 | 0.06 |
| Zr | 46.50 | 60.40 | 83.60 | 76.00 | 69.00 | 124.00 | 119.00 | 89.00 | 75.00 | 22.00 | 22.00 | 23.00 | 23.00 | 28.20 | 32.70 |
| Hf | 1.60 | 2.03 | 2.63 | 2.10 | 1.90 | 3.30 | 3.00 | 2.40 | 2.00 | 0.90 | 1.00 | 0.90 | 1.00 | 1.26 | 1.46 |
| Th | 1.71 | 2.25 | 3.11 | 2.47 | 2.63 | 3.16 | 2.90 | 2.76 | 2.96 | 0.47 | 0.48 | 0.54 | 0.49 | 0.71 | 0.73 |
| U | 0.42 | 0.62 | 0.88 | 0.73 | 0.76 | 0.95 | 0.89 | 0.83 | 0.86 | 0.14 | 0.15 | 0.16 | 0.15 | 0.20 | 0.23 |
| Pb | 4.02 | 14.50 | 5.58 | 5.00 | 5.00 | 5.00 | 5.00 | 5.00 | 5.00 | 5.00 | 5.00 | 5.00 | 5.00 | 18.50 | 10.70 |

Mg# = 100 × [Mg2+ / (Mg2+ + TFe2+)]; m/f = Mg2+ / (TFe2+ + Mn2+); The data with "*" are cited from Wang et al. (2014b).

The values of (La/Nb)$_{PM}$ and (Th/Ta)$_{PM}$ are markedly different between the upper and lower crust, meaning they can be used to identify the source of contaminants (Neal et al., 2002). In Fig. 14, the data plot near the average values of the upper crust, indicating that the materials responsible for contamination originated from the upper crust. The high initial Sr isotopic ratios and negative $\varepsilon_{Nd}(t)$ values of our samples are indicative of crustal contamination. The similar scenarios have also been observed in other intrusions bearing Ni–Cu sulfide ores, such as Norilsk in Russia (Arndt et al., 2003), Limahe in Sichuan Province of China (Zhang et al., 2009a), and Baimazhai in Yunnan Province of China (Wang and Zhou, 2006).

The positive $\varepsilon_{Hf}(t)$ values of the zircon grains indicate they were sourced from the depleted mantle, although the high initial Sr isotopic ratios and negative $\varepsilon_{Nd}(t)$ values are characteristic of enriched mantle. This result rises because the isotopic systems of lithophile elements such as Sr and Nd are more sensitive indicators of crustal contamination since lithophile elements are more abundant in the crust than in the mantle. In addition, during partial melting and devolatilization related to ore formation, the host magma may selectively combine with unstable components such as crustal sulfur (Lesher and Burnham, 2001), with the result that the magma becomes selectively contaminated by crustal sulfides (Ripley et al., 1999; Ling, 2014). Therefore, it is reasonable to expect that the whole-rock Sm–Nd data were more affected by crustal sulfides than the zircon grains from the Xiarihamu mafic–ultramafic complexes, which formed during the early stages of magma crystallization. The selective contamination of magma can explain the decoupling of Hf and Sr–Nd isotopes.
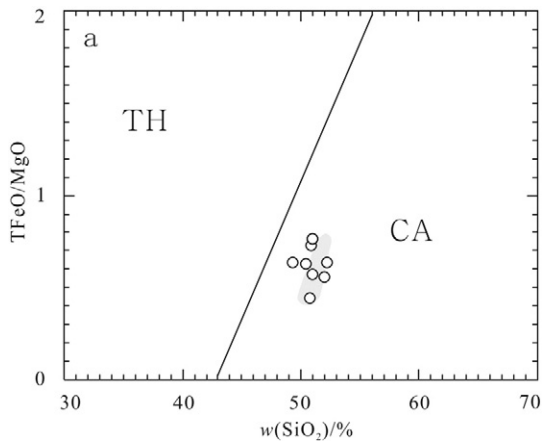
**Fig. 9.** SiO$_2$ vs. TFeO/MgO diagram of the Xiarihamu II mafic–ultramafic complex. (TH—tholeiitic series; CA—calc-alkali series;)

Previous studies have shown that fluid released during dehydration of a subducting plate affects the content of fluid-soluble elements in the overlying mantle wedge but that high field-strength elements (HFSE) are relatively depleted owing to their low solubility in fluids (Regelous et al., 1997). Therefore, metasomatism in the mantle wedge is characterized by strong enrichment in LILE and depletion in HFSE, as observed in the Xiarihamu mafic–ultramafic complexes. On a diagram of Th/Yb vs. Nb/Yb the gabbro samples all diverge from the MORB–OIB evolution line (Fig. 15a), plotting near the volcanic arc array, reflecting the influence of subduction components (Pearce and Peate, 1995). Trace element ratios such as Ba/Th, Th/Nb, Ba/La, Th/Yb, Nb/Zr, and Th/Zr can effectively discriminate between an aqueous fluid and a subduction zone sediment component. Samples from the Xiarihamu II mafic–ultramafic complex have relatively constant Th/Nb and Th/Yb ratios (0.96–1.2 and 0.96–1.64, respectively). Samples from the Xiarihamu I mafic–ultramafic complex also have relatively constant Th/Nb and Th/Yb ratios (0.77–1.2 and 0.40–0.53, respectively). Fig. 15b and c shows that abundant aqueous fluids entered the mantle source region of the parent magma to the complex (Woodhead et al., 2001; Hanyu et al., 2006; Tian et al., 2011). On diagrams of La/Nb vs. Th/Yb and Nb/Zr vs. Th/Zr (Fig. 15d), the trends of the samples are consistent with subduction-fluid metasomatism. The above features indicate that the source region contained a large amount of aqueous fluid.

In conclusion, we consider that the parental magmas that fed the Xiarihamu intrusions were derived from a metasomatised, asthenospheric mantle source that had previously been modified by subduction-related fluids.

### 6.2. Constraints on ore genesis

Sulfide melt and silicate magma are expected to separate from each other in magmatic melts, resulting in mineralization. Sulfide liquids are enriched in chalcophile elements that become differentiated due to gravitational sinking, leading to sulfide enrichment and mineralization. The most important factor for sulfide-mineral mineralization is the attainment of saturation in magmas (Brugmann et al., 1993; Mavrogenes and O'Neill, 1999). A negative correlation exists between solubility and magma pressure: S tends to become unsaturated as magma pressure decreases during ascent. Without external influences, magmatic sulfur cannot generate the saturation required to form large-scale Cu–Ni sulfide deposits (Naldrett, 2004). Previous studies have reported that ore-bearing basic intrusions have experienced crustal contamination, and therefore proposed that added crustal sulfur is an important source of sulfur over-saturation in magmas (Ripley, 1981; Grinenko, 1985; Naldrett, 1989). As mentioned above, the Xiarihamu intrusions experienced significant crustal contamination. S isotopes obtained from sulfide minerals in the Xiarihamu II altered massive gabbro (Table 5) have a small range of δ$^{34}$S values of 4.9%–6.1% that lie outside of mantle values ($-2\% \pm 2\%$), and the δ$^{34}$S values of sulfide minerals in intrusion I are 3.4%–7.6%, also outside the range of mantle values. This result strongly indicates that the Xiarihamu sulfur isotopic composition is crust-derived and that assimilated crustal sulfur was responsible for generating S saturation in the Xiarihamu deposit.

Most Ni–Cu sulfide deposits occur in relatively small, sill-and dike-like bodies that have been interpreted as magmatic conduits (Naldrett, 2004; Barnes and Lightfoot, 2005; Zhang et al., 2009a). While the total volume of all the intrusions in the Xiarihamu complex is quite small, they have reasonably high sulfide contents. The ore bodies are located mainly at the base of the intrusions. The upper ore is disseminated while the lower–middle part and base are densely disseminated and locally densely massive, indicating that gravity played an important role during sulfide-mineral precipitation and subsequent ore formation. It is suggested that the primary magma that fed the Xiarihamu intrusions hosting the Cu–Ni sulfide deposits, experienced significant contamination from upper crustal materials during ascent.
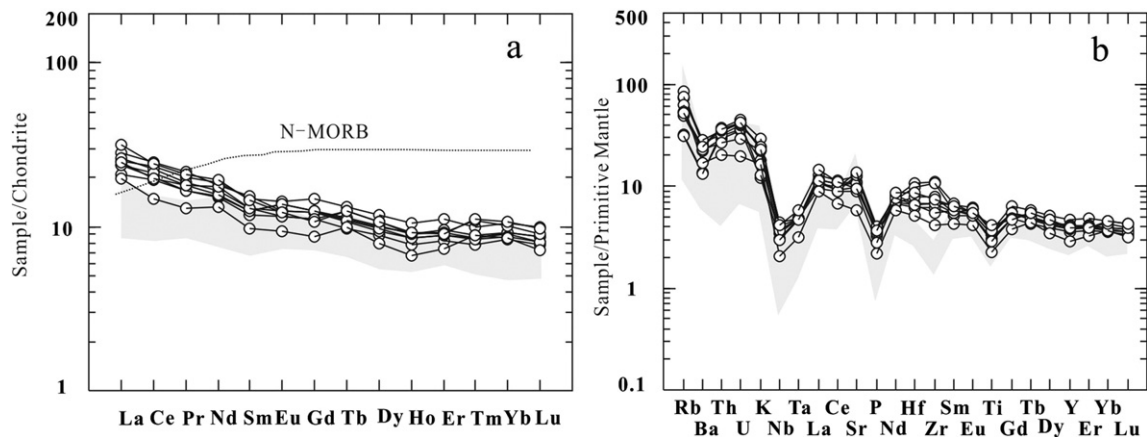


**Fig. 10.** a. Chondrite-normalized REE patterns of the Xiarihamu II mafic–ultramafic complex (chondrite REE values from Boynton, 1984). b Primitive mantle-normalized element spider diagrams of the Xiarihamu II mafic–ultramafic complex (primitive mantle values from Sun and McDonough, 1989).

**Table 3**
Zircon Lu–Hf isotopic compositions of samples in Xiarihamu mafic–ultramafic complexes.

| Analysis | $^{176}Hf/^{177}Hf$ | $2\sigma$ | $^{176}Lu/^{177}Hf$ | $2\sigma$ | $^{176}Yb/^{177}Hf$ | $2\sigma$ | $\varepsilon_{Hf}(0)$ | $\varepsilon_{Hf}(t)$ | $2\sigma$ | $t_{DM1}$ | $t_{DM2}$ | $f_{Lu/Hf}$ |
|---|---|---|---|---|---|---|---|---|---|---|---|---|
| XRHM-II-N1-1 | 0.282811 | 0.000047 | 0.001573 | 0.000087 | 0.06166 | 0.002417 | 1.4 | 10.3 | 1.8 | 634 | 713 | −0.95 |
| XRHM-II-N1-2 | 0.282732 | 0.000035 | 0.001092 | 0.000154 | 0.04316 | 0.005578 | −1.4 | 7.6 | 1.4 | 739 | 862 | −0.97 |
| XRHM-II-N1-3 | 0.282883 | 0.00002 | 0.001425 | 0.000043 | 0.05095 | 0.001526 | 3.9 | 12.9 | 0.9 | 530 | 570 | −0.96 |
| XRHM-II-N1-4 | 0.282912 | 0.000013 | 0.002224 | 0.000033 | 0.08733 | 0.001670 | 5 | 13.7 | 0.7 | 497 | 523 | −0.93 |
| XRHM-II-N1-5 | 0.282839 | 0.000031 | 0.001706 | 0.000017 | 0.06050 | 0.000818 | 2.4 | 11.2 | 1.2 | 596 | 660 | −0.95 |
| XRHM-II-N1-6 | 0.282721 | 0.000049 | 0.00209 | 0.000006 | 0.08188 | 0.000021 | −1.8 | 6.9 | 1.8 | 775 | 900 | −0.94 |
| XRHM-II-N1-7 | 0.282864 | 0.000025 | 0.002054 | 0.000046 | 0.07784 | 0.002207 | 3.3 | 12 | 1 | 565 | 615 | −0.94 |
| XRHM-II-N1-8 | 0.282853 | 0.000034 | 0.001842 | 0.000043 | 0.06146 | 0.001449 | 2.9 | 11.7 | 1.3 | 578 | 634 | −0.94 |
| XRHM-II-N1-9 | 0.282881 | 0.000041 | 0.002359 | 0.000051 | 0.08558 | 0.002565 | 3.8 | 12.5 | 1.6 | 546 | 588 | −0.93 |
| XRHM-II-N1-10 | 0.282779 | 0.000026 | 0.001418 | 0.000012 | 0.04572 | 0.000554 | 0.2 | 9.2 | 1.1 | 678 | 775 | −0.96 |
| XRHM-II-N1-11 | 0.28287 | 0.000029 | 0.001779 | 0.000101 | 0.05610 | 0.003428 | 3.5 | 12.3 | 1.2 | 553 | 600 | −0.95 |
| XRHM-I-N1-1* | 0.282 661 | 0.000 028 | 0.000 709 | 0.000 005 | 0.028 056 | 0.000 182 | −3.9 | 5.2 | 1.1 | 830 | 995 | −0.98 |
| XRHM-I-N1-2* | 0.282 729 | 0.000 030 | 0.001 094 | 0.000 027 | 0.045 714 | 0.000 437 | −1.5 | 7.5 | 1.2 | 743 | 869 | −0.97 |
| XRHM-I-N1-3* | 0.282 719 | 0.000 025 | 0.001 012 | 0.000 030 | 0.041 571 | 0.000 769 | −1.9 | 7.2 | 1.1 | 755 | 886 | −0.97 |
| XRHM-I-N1-4* | 0.282 743 | 0.000 031 | 0.001 030 | 0.000 004 | 0.045 219 | 0.000 830 | −1 | 8 | 1.2 | 722 | 839 | −0.97 |
| XRHM-I-N1-5* | 0.282 638 | 0.000 024 | 0.000 629 | 0.000 003 | 0.025 232 | 0.000 462 | −4.7 | 4.4 | 1 | 861 | 1040 | −0.98 |
| XRHM-I-N1-6* | 0.282 684 | 0.000 022 | 0.001 000 | 0.000 019 | 0.036 247 | 0.000 747 | −3.1 | 5.9 | 1 | 804 | 955 | −0.97 |
| XRHM-I-N1-7* | 0.282 665 | 0.000 038 | 0.000 811 | 0.000 010 | 0.037 196 | 0.000 520 | −3.8 | 5.3 | 1.4 | 827 | 990 | −0.98 |
| XRHM-I-N1-8* | 0.282 833 | 0.000 022 | 0.001 965 | 0.000 014 | 0.084 957 | 0.000 646 | 2.1 | 10.9 | 0.9 | 610 | 677 | −0.94 |
| XRHM-I-N1-9* | 0.282 740 | 0.000 027 | 0.001 134 | 0.000 015 | 0.043 139 | 0.000 921 | −1.1 | 7.9 | 1.1 | 727 | 846 | −0.97 |
| XRHM-I-N1-10* | 0.282 628 | 0.000 036 | 0.000 633 | 0.000 025 | 0.023 908 | 0.000 928 | −5.1 | 4 | 1.4 | 875 | 1060 | −0.98 |
| XRHM-I-N1-11* | 0.282 654 | 0.000 028 | 0.000 625 | 0.000 010 | 0.025 745 | 0.000 598 | −4.2 | 5 | 1.1 | 839 | 1009 | −0.98 |
| XRHM-I-N1-12* | 0.282 651 | 0.000 028 | 0.000 653 | 0.000 016 | 0.027 018 | 0.000 872 | −4.3 | 4.9 | 1.1 | 843 | 1014 | −0.98 |
| XRHM-I-N1-13* | 0.282 681 | 0.000 031 | 0.000 934 | 0.000 016 | 0.037 601 | 0.000 572 | −3.2 | 5.8 | 1.2 | 807 | 960 | −0.97 |

Mg# = 100 × [Mg2+ / (Mg2+ + TFe2+)]; m/f = Mg2+ / (TFe2+ + Mn2+); The data with "*" are cited from Wang et al. (2014b).
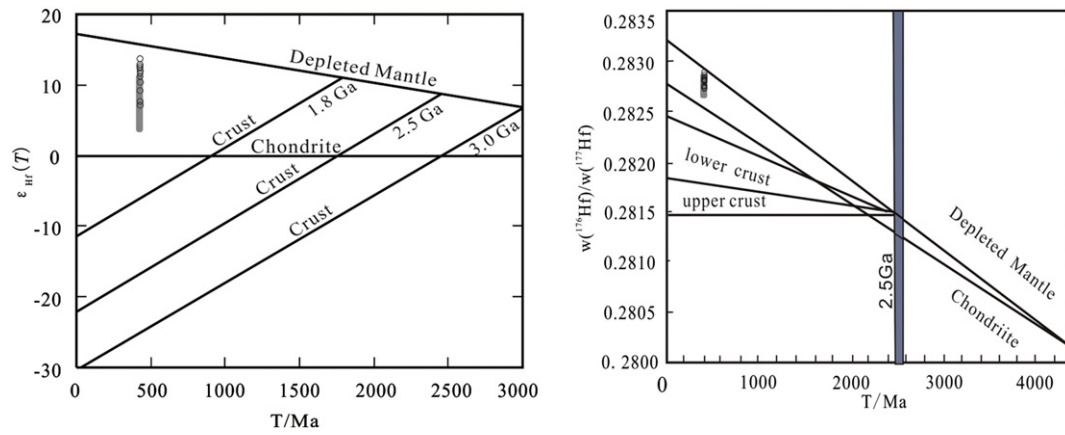
Fig. 11. Zircon Hf isotopic features for gabbro in Xiarihamu II mafic–ultramafic complex.

This resulted in the assimilation of sulfur-rich rocks and the formation of a sulfide-rich melt that precipitated in the widest part of the conduit or in a shallowly inclined part of the conduit due its high density. Magma continued to ascend due to its low density, experiencing repeated sulfide enrichment as magma flowed continuously through the conduit. These intrusions have been interpreted to represent conduits through which both silicate melt and sulfide liquid ascended (Zhang et al., 2009b).

### 6.3. Tectonic setting

Previous studies have shown that the opening and expansion of the early Paleozoic ocean in the EKO occurred before the Pre-Cambrian (Yang et al., 1996; Lu, 2002; Feng et al., 2010a,b). Subsequently, the Proto-Tethys Ocean began subducting to the north and south. With the intensification of subduction, a series of island arcs and an active continental margin formed. Diorite from the Yaziquan arc, located in the Qimatage area of the EKO, yields a magmatic crystallization age of ~480 Ma (Cui et al., 2011). Basaltic–dacitic lava that occurs near the Middle Kunlun Fault yields a magmatic crystallization age of ~448 Ma (Chen et al., 2002a,b). However, LA–ICP–MS zircon U–Pb analyses yielded a magmatic crystallization age of 438.2 ± 2 Ma for the Huxiaoqin hornblende pyroxenite (Liu et al., 2013a,b) and 436 ± 1 Ma for the Qingshuiquan diabase dykes located in the Middle EKO. These mafic rocks and basic dikes, which are located along the Middle Kunlun suture zone, may represent the youngest phase of magmatism related to the early Paleozoic subduction of oceanic crust (Liu et al.,

2013a,b). Rapakivi and monzonitic granite in the EKO that are related to continent–continent collision yield magmatic crystallization ages of 428.5 ± 2.2 Ma and 430.8 ± 1.7 Ma, respectively (Cao et al., 2011). Eclogite-facies metamorphism, related to continent–continent collision in the EKO, has been dated at ~428 Ma (Meng et al., 2013), and peak medium-pressure (epidote) amphibolite-facies metamorphism has been dated at ~427 Ma (Chen et al., 2002a,b). In addition, the Bashierxi A-type granite from the western part of the EKO was emplaced at ~432 Ma (Gao et al., 2010). Collectively, these dates indicate that strong continent–continent collision finished at ~430 Ma, after a post-collisional extensional stage.

Zircon U–Pb age dating of this study indicates that the magmatic crystallization age of the Xiarihamu II mafic–ultramafic complex is 424 ± 1 Ma, which is within error of the age of the Xiarihamu I mafic–ultramafic complex (423 ± 1 Ma; Wang et al., 2014a,b). Other granitic intrusions in the region have similar ages: the Wulanwuzhu granite, located in the Qimantage area of the western EKO, has a magmatic crystallization age of 421.2 ± 1.9 Ma; the Naleguole biotite monzogranite has a magmatic crystallization age of 420.6 ± 2.6 Ma (Hao et al., 2014); and the Wulonggou monzonitic granite, located in the eastern EKO, has a magmatic crystallization age of 420–418 Ma (Lu et al., 2013). Zircon SIMS U–Pb dating yielded an age of 422 ± 3 Ma for the Baiganhu A-type moyite and an age of 421 ± 3.7 Ma for the Baiganhu monzonitic granite (Li et al., 2012a,b).

The above granites include a strongly peraluminous granite and a high-K calc-alkaline I-type granite. Mafic–ultramafic rocks and various

**Table 4**
Sr–Nd isotope of Xiarihamu mafic–ultramafic complexes.

| Samples | XRHM-II-B1 | XRHM-II-B2 | XRHM-II-B13 | XRHM-II-B4 | XRHM-II-B5 | XRHM-I-B1 | XRHM-I-B2 | XRHM-I-B3 | XRHM-I-B4 |
|---|---|---|---|---|---|---|---|---|---|
| Sm [ppm] | 3.37 | 2.78 | 2.82 | 2.87 | 2.99 | 1 | 0.53 | 0.76 | 0.43 |
| Nd[ppm] | 11.86 | 10.67 | 11 | 11.27 | 10.93 | 3.89 | 2.24 | 2.72 | 1.72 |
| $^{147}Sm/^{144}Nd$ | 0.1729 | 0.1586 | 0.156 | 0.155 | 0.1665 | 0.1565 | 0.144 | 0.1701 | 0.1522 |
| $^{143}Nd/^{144}Nd$ | 0.512464 | 0.512466 | 0.512488 | 0.512475 | 0.512459 | 0.512363 | 0.512406 | 0.512435 | 0.512418 |
| 2s | 0.000012 | 0.000009 | 0.000012 | 0.000013 | 0.000013 | 0.000013 | 0.00001 | 0.000012 | 0.000013 |
| $(^{143}Nd/^{144}Nd)i$ | 0.511984 | 0.512026 | 0.512055 | 0.512045 | 0.511997 | 0.511931 | 0.512008 | 0.511965 | 0.511997 |
| εNd(t) | −2.1 | −1.3 | −0.7 | −0.9 | −1.9 | −3.2 | −1.7 | −2.5 | −1.9 |
| Rb [ppm] | 25.91 | 22.52 | 45.59 | 23.34 | 52.02 | 8.08 | 13.44 | 13.46 | 5.24 |
| Sr [ppm] | 233.29 | 219.18 | 322.51 | 227.79 | 303.78 | 54.74 | 14.3 | 21.3 | 8.36 |
| $^{87}Rb/^{86}Sr$ | 0.3216 | 0.2975 | 0.4093 | 0.2967 | 0.4958 | 0.4274 | 2.7215 | 1.8298 | 1.8149 |
| $^{87}Sr/^{86}Sr$ | 0.71039 | 0.710401 | 0.710672 | 0.71 | 0.711608 | 0.713501 | 0.719474 | 0.716 | 0.715114 |
| 2s | 0.000012 | 0.000011 | 0.000012 | 0.00001 | 0.000011 | 0.000012 | 0.000011 | 0.000012 | 0.000013 |
| $(^{87}Sr/^{86}Sr)i$ | 0.708448 | 0.708604 | 0.7082 | 0.708208 | 0.708614 | 0.710932 | 0.703117 | 0.705002 | 0.704205 |
| εSr(t) | 56.5 | 58.8 | 53 | 53.1 | 58.9 | 91.8 | −19.1 | 7.6 | −3.7 |
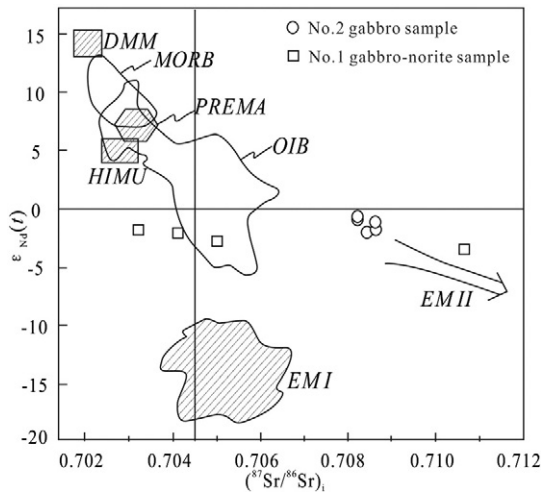
**Fig. 12.** ($^{87}$Sr–$^{86}$Sr)i vs. εNd(t) diagram for Xiarihamu mafic–ultramafic complexes (after Zindler and Hart, 1986).
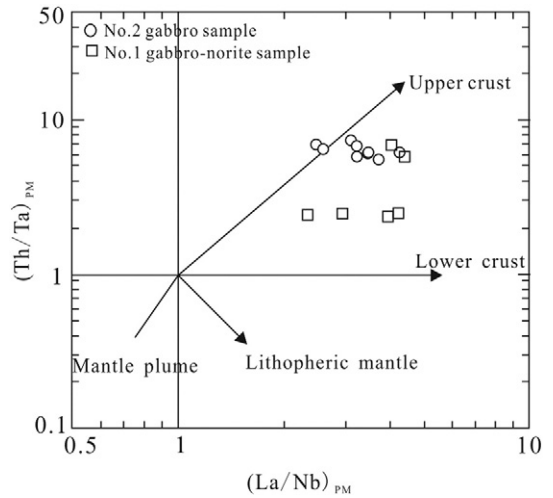


**Fig. 14.** (La/Nb)$_{PM}$ vs. (Th/Ta)$_{PM}$ diagrams for Xiarihamu mafic–ultramafic complexes (after Neal et al., 2002).

types of granites formed simultaneously in the EKO during the late Silurian, indicating strong crust–mantle interaction. Early–Middle Triassic A-type granites (the EKO Bigou syenogranite has a magmatic crystallization age of 391 ± 3 Ma, Liu et al., 2013a,b; the EKO Lalingzaohuo monzogranite has a magmatic crystallization age of 396.2 ± 2 Ma, Chen et al., 2013) mark the ending of the Proto-Tethys tectonic evolution in the EKO during the Middle Devonian.

Previous studies have shown that magma formed in a post-collisional extensional environment may have geochemical signatures of an island arc or active continental margin (Aldanmaz et al., 2000; Wang et al., 2004; Zhang et al., 2003); thus, the source region can retain the characteristics of previously subducted oceanic crust, such as a strong enrichment in LILE (e.g., Rb, Ba, Th, U, and K) and depletions in Nb, Ta, P, and Ti.

In conclusion, the Xiarihamu mafic–ultramafic complexes probably formed in a post-collisional, extensional regime. The southern basaltic oceanic plateau of the southeast Kunlun composite accretion belt collided with the northern Mid-east Kunlun uplifted basement and granitic belt during the closure of the Proto-Tethys Ocean. Because the basalt plateau is very thick (25–36 km), it impeded further subduction of oceanic crust. However, oceanic crust that was already subducted continued to sink, which ultimately led to slab break-off and the formation of a slab window. The slab window induced the upwelling

of deep asthenosphere, which led to decompression melting. The parental magma experienced significant crustal contamination, either during ascent or emplacement, triggering S over-saturation that resulted in the dissolution of sulfide minerals, the precipitation of sulfide minerals, and sulfide enrichment in the magma. The silicate magma continued to ascend due to buoyancy, eventually forming the Xiarihamu mafic–ultramafic complexes and the Xiarihamu Ni–Cu sulfide deposit.

## Conclusion

(1) Xiarihamu II mafic–ultramafic complex formed in a post-collisional, extensional regime.

(2) The parental magmas that fed the Xiarihamu intrusions were derived from a metasomatised, asthenospheric mantle source that had previously been modified by subduction-related fluids.

(3) The parental magma experienced significant crustal contamination, either during ascent or emplacement, triggering S over-saturation that resulted in the precipitation of sulfide minerals, and sulfide enrichment in the magma. The silicate magma continued to ascend due to buoyancy, eventually forming the Xiarihamu mafic–ultramafic complexes and the Xiarihamu Ni–Cu sulfide deposit.
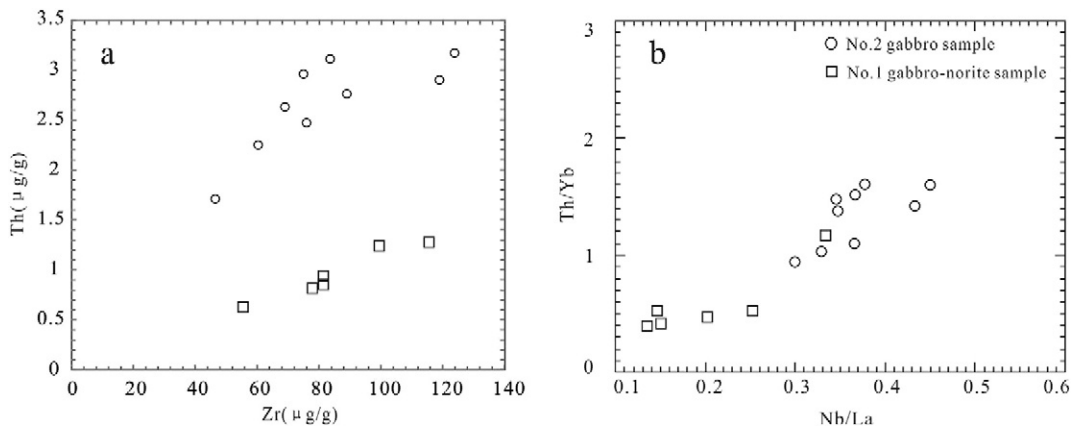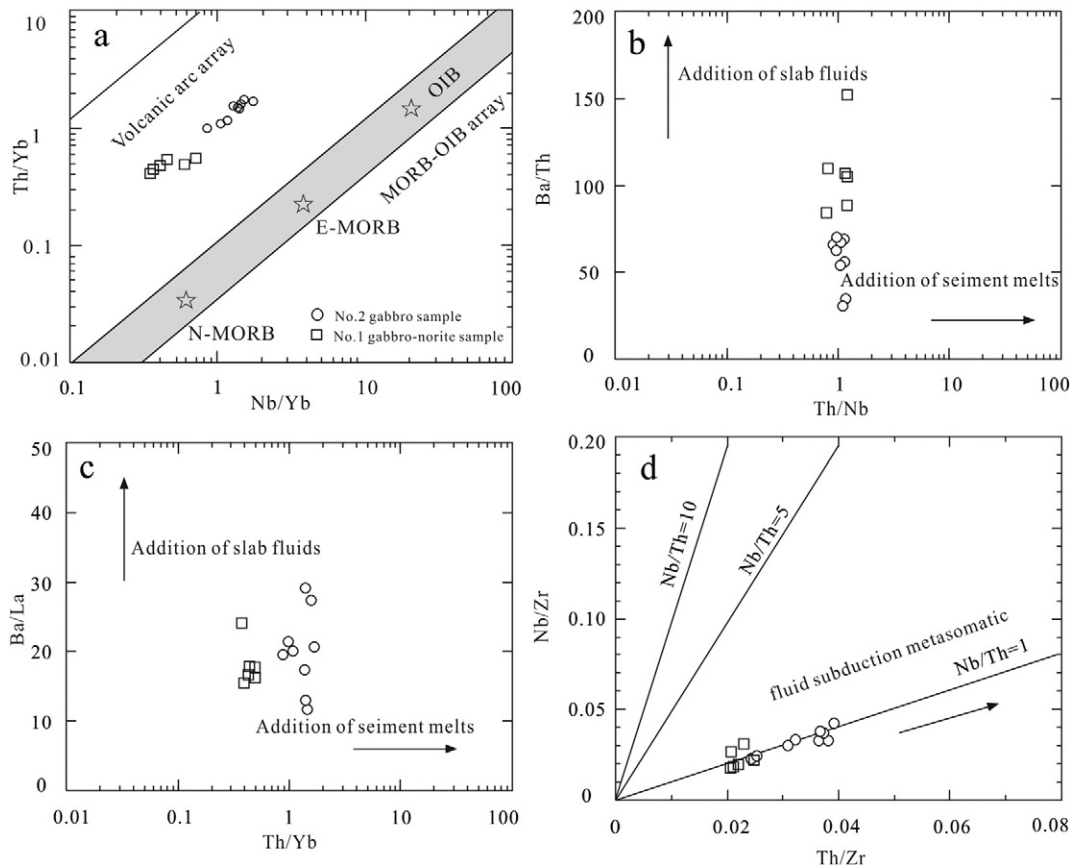


**Fig. 13.** Plots of selected trace element for checking contamination of the Xiarihamu mafic–ultramafic complexes.

**Fig. 15.** Nb/Yb vs. Th/Yb (a), Th/Nb vs. Ba/Th (b), Th/Yb vs. Ba/La (c),Th/Zr vs. Nb/Zr (d) diagrams of the Xiarihamu mafic–ultramafic complexes (a after Pearce, 2008; b, c after Hanyu et al., 2006; d after Woodhead et al., 2001).

**Table 5**
Sulfur isotopic compositions of sulfides from Xiarihamu Cu-Ni deposit.

| Ser. no. | Sample | Position | Mineral | $\delta^{34}$SCDT (‰) |
|---|---|---|---|---|
| 1 | XRHM-II-S1 | II intrusion | Pyrrhotite | 5.7 |
| 2 | XRHM-II-S1 | | Chalcopytite | 6.1 |
| 3 | XRHM-II-S2 | | Pyrrhotite | 4.9 |
| 4 | XRHM-II-S2 | | Chalcopytite | 6.1 |
| 5 | XRHM-II-S3 | | Pyrrhotite | 5.6 |
| 6 | XRHM-II-S3 | | Chalcopytite | 6 |
| 7 | XRHM-II-S4 | I intrusion | Pentlandite | 4 |
| 8 | XRHM-II-S5 | | Pentlandite | 5.2 |
| 9 | XRHM-II-S6 | | Pentlandite | 6 |
| 10 | XRHM-II-S6 | | Chalcopytite | 6.6 |
| 11 | XRHM-II-S7 | | Pentlandite | 5.6 |
| 12 | XRHM-II-S7 | | Chalcopytite | 5.8 |
| 13 | XRHM-II-S8 | | Pentlandite | 6 |
| 14 | XRHM-II-S8 | | Chalcopytite | 6.5 |
| 15 | XRHM-II-S9 | | Pentlandite | 5.7 |
| 16 | XRHM-II-S9 | | Chalcopytite | 5.7 |
| 17 | XRHM-II-S10 | | Pentlandite | 5.3 |
| 18 | XRHM-II-S10 | | Pyrrhotite | 7.6 |
| 19 | XRHM-II-S10 | | Chalcopytite | 5.8 |
| 20 | XRHM-II-S11 | | Pentlandite | 3.5 |
| 21 | XRHM-II-S12 | | Pentlandite | 3.4 |
| 22 | XRHM-II-S12 | | Chalcopytite | 4.6 |
| 23 | XRHM-II-S13 | | Pentlandite | 3.8 |

## Acknowledgments

## References

Aldanmaz, E., Pearce, J.A., Thirlwall, M.F., Mitchell, J.G., 2000. Petrogenetic evolution of late Cenozoic, post-collision volcanism in western Anatolia, Turkey. J. Volcanol. Geotherm. Res. 102 (1), 67–95.

Arndt, N.T., Czamanske, G., Walker, R.J., Chauvel, C., Fedorenko, V., 2003. Geochemistry and origin of the intrusive hosts of the Noril'sk-Talnakh Cu–Ni–PGE sulfide deposits. Econ. Geol. 98, 495–515.

Baker, J.A., Menzies, M.A., Thirlwall, M.F., Thirlwall MacPherson, C.G., 1997. Petrogenesis of Quaternary intraplate volcanism,Sana'a,Yemen:Implications for plume—lithosphere interaction and polybaric melt hybridization. J. Petrol. 38 (10), 1359–1390.

Barnes, S.J., Lightfoot, P.C., 2005. Formation of magmatic nickel sulfide ore deposits and processs affecting their copper and platinum group element contents. Econ. Geol. 100th Anniv. 179–213.

Boynton, W.V., 1984. Geochemistry of the rare earth elements: meteorite studies. In: Henderson, P. (Ed.), Rare Earth Elements Geochemistry. Elservier, Amsterdam, pp. 63–114.

Brugmann, G.E., Naldrett, A.J., Asif, M., 1993. Siderophile and chalcophile metals as tracers of the evolution of the Siberian traps in the Noril'sk region, Russia. Geochim. Cosmochim. Acta 57, 2001–2018.

Campbell, I.H., 2002. Implications of Nb/U, Th/U and Sm/Nd in plume magma for the relationship between continental and oceanic crust formation and the depleted mantle. Geochim. Cosmochim. Acta 66 (9), 1651–1661.

Campbell, I.H., Griffiths, R.W., 1993. The evolution of the mantle's chemical structure. Lithos 30 (3), 389–399.

Cao, S.T., Liu, X.K., Ma, Y.S., Li, Y.J., Ma, Y.L., 2011. The discovery of Early Silurian intrusive rocks in Qimantage area and its geological significance. Qinghai Sci. Technol. 5, 26–30 (in Chinese).

Chen, N.S., He, L., Sun, M., Wang, G.C., Zhang, K.X., 2002b. Precise timing of the Early Paleozoic metamorphism and thrust deformation in the Eastern Kunlun Orogen. Chin. Sci. Bull. 47 (13), 1130–1133.

Chen, F., Hegner, E., Todt, W., 2000. Zircon ages, Nd isotopic and chemical compositions of orthogneissses from the Black Forest, Gemany—evidence for a Cambrian magmatic arc. Int. J. Earth Sci. 88, 791–802.

Chen, F., Satir, M., Ji, J., Zhong, D., 2002a. Nd-Sr-Pb isotopes of Tengchong Cenozoic volcanic rocks from western Yunnan, China: evidence for an enriched-mantle source. J. Asian Earth Sci. 21, 39–45.

Chen, J., Xie, Z.Y., Li, B., Tan, S.X., Ren, H., Zhang, Q.M., Li, Y., 2013. Petrogenesis of Devonian intrusive rocks in Lalingzaohuo area, Eastern Kunlun, and its geological significance. Mineral. Petrol. 33 (2), 26–34 (in Chinese with English abstract).

Cui, M.H., Meng, F.C., Wu, X.K., 2011. Early Ordovician island arc of Qimantag Mountain, eastern Kunlun: evidences from geochemistry, Sm–Nd isotope and geochronology of intermediate-basic igneous rocks. Acta Petrol. Sin. 27 (11), 3365–3379 (in Chinese with English abstract).

Feng, C.Y., Li, D.S., Wu, Z.S., Li, J.H., Zhang, Z.Y., Zhang, A.K., Shu, X.F., Su, S.S., 2010a. Major types, tim-space distribution and metallogenesis of polymetallic deposits in the Qimantage Metallogenic Belt, Eastern Kunlun area. Northwestern Geology 43 (4), 10–17 (in Chinese with English abstract).

Feng, J.Y., Pei, X.Z., Yu, S.L., Ding, S.P., Li, R.B., Sun, Y., Zhang, Y.F., Li, Z.C., Chen, Y.X., Zhang, X.F., Chen, G.C., 2010b. The discovery of the mafic- ultramafic mélange in Kekesha area of Dulan County, East Kunlun region, and its LA–ICP-MS zircon U–Pb age. Geol. China 37 (1), 28–38 (in Chinese with English abstract).

Feng, C.Y., Zhang, D.Q., Wang, F.C., She, H.Q., Li, D.X., Wang, Y., 2004. Multiple orogenic processes and geological characteristics of the major orogenic gold deposits in East Kunlun area, Qinghai Province. Acta Geosci. Sin. 25 (4), 415–422 (in Chinese with English abstract).

Fisher, C.M., Vervoot, J.D., Hanchar, J.M., 2014. Guidelines for reporting zircon Hf istopic data by LA–ICPMS and potential pitfalls in the interpretation of these data. Chem. Geol. 363, 125–133.

Furman, T.Y., Bryce, J.G., Karson, J., Iotti, A., 2004. East African rift system (EARS) plume structure: insight from quarternary mafic lavas of Turkana, Kenya. J. Petrol. 45, 1069–1088.

Gao, X.F., Xiao, P.X., Xie, C.R., Fan, L.Y., Guo, L., Xi, R.G., 2010. Zircon LA–ICP-MS U–Pb dating and geological significance of bashierxi granite in the eastern Kunlun area, China. Geol. Bull. China 29 (7), 1001–1008.

Grinenko, L.N., 1985. Sources of sulfur of the nickeliferous and barren gabbro-dolerite intrusions of the northwest Siberian platform. Int. Geol. Rev. 695-708.

Hanyu, T., Tatsumi, Y., Nakai, S.I., Chang, Q., Miyazaki, T., Sato, K., Tani, K., Shibata, T., Yoshida, T., 2006. Contribution of slab melting and slab dehydration to magmatism in the NE Japan arc for the last 25 Myr: constraints from geochemistry. Geochem. Geophys. Geosyst. 7 (8). http://dx.doi.org/10.1029/2005GC001220.

Hao, N.N., Yuan, W.M., Zhang, A.K., Cao, J.H., Chen, X.N., Feng, Y.L., Li, X., 2014. Late silurian to Early Devonian Granitoids in the Qimantage Area, East Kunlun Mountains: LA–ICP-MS zircon U–Pb ages, geochemical features and geological seting. Geol. Rev. 60 (1), 201–215 (in Chinese with English abstract).

Hart, S.R., 1988. Heterogeneous mantle domains: signatures, genesis and mixing chronologies. Earth Planet. Sci. Lett. 90 (3), 273–296.

Hofmann, A.W., 1988. Chemical differentiation of the earth: the relationship between mantle, continental crust, and oceanic crust. Earth Planet. Sci. Lett. 90, 297–314.

Hou, K.J., Li, Y.H., Tian, Y.R., 2009. In situ U–Pb zircon dating using laser ablation–multi ion counting–ICP-MS. Mineral Deposits 28 (4), 481–492 (in Chinese with English abstract).

Hu, Z.C., Liu, Y.S., Gao, S., Liu, W.G., Zhang, W., Tong, X.R., Lin, L., Zong, K.Q., Li, M., Chen, H.H., Zhou, L., Yang, L., 2012. Improved in situ Hf isotope ratio analysis of zircon using newly designed X skimmer cone and jet sample cone in combination with the addition of nitrogen by laser ablation multiple collector ICP-MS. J. Anal. Atom. Spectrom. 27 (9), 1391–1399.

Huang, J.Q., Chen, G.M., Chen, B.W., 1984. Preliminary analysis of the Tethys-Himalayan tectonic Dodoma. Acta Geol. Sin. 58 (1), 1–17 (in Chinese).

Jahn, B.M., Condie, K.C., 1995. Evolution of the kaapvaal craton as viewed from geochemical and Sm–Nd isotopic analyses of intractationic pelites. Geochim. Cosmochim. Acta 59 (11), 2239–2258.

Jiang, C.Y., Ling, J.L., Zhou, W., Du, Q., Wang, Z.X., Fan, Y.Z., Song, Y.F., Song, Z.B., 2015. Petrogenesis of the Xiarihamu Ni-bearing layered mafic-ultramafic intrusion, East Kunlun: implication for its extensional island arc environment. Acta Petrol. Sin. 31 (4), 1117–1136.

Jiang, C.F., Wang, Z.Q., Li, M.T., 2000. Opening–closing Tectonics of the Central Orogenic Belt. Geological Publishing House, Beijing (in Chinese).

Jiang, C.F., Yang, J.S., Fen, B.G., 1992. Opening–Closing Tectonics of the Kunlun Mountain. Geological Publishing House, Beijing (in Chinese).

Lesher, C.M., Burnham, O., 2001. Multicomponent element and isotopic mixing in Ni–Cu–(PGE) ores at Kamabalda, Western Australia. Can. Mineral. 39, 421–446.

Li, G.C., Feng, C.Y., Wang, R.J., Ma, S.C., Li, H.M., Zhou, A.S., 2012b. SIMS zircon U–Pb age, petrochemistry and tectonic implications of granitoids in northeastern Baiganhue W–Sn Orefield, Xinjiang. Acta Geosci. Sin. 33 (2), 216–226 (in Chinese with English abstract).

Li, S.J., Sun, F.Y., Gao, Y.W., Zhao, J.W., Li, L.S., Yang, Q.A., 2012a. The theoretical guidance and the practice of small intrusions forming large deposits—the enlightenment and significance for searching breakthrough of Cu–Ni sulfide deposit in Xiarihamu, East Kun lun, Qinghai. Northwest. Geol. 45 (4), 185–191 (in Chinese with English abstract).

Ling, J.L., 2014. Petrogenesis of mafic–ultramafic intrusions and minerogenesis of nickel deposit in the periphery of Qaidam block, Qianghai, China. Chang'an University, Xi'an, China, pp. 1–178.

Liu, B., Ma, C.Q., Guo, P., Zhang, J.Y., Xiong, F.H., Huang, J., Jiang, H.A., 2013b. Discovery of the Middle Devonian A-type granite from the Eastern Kunlun Orogen and its tectonic implications. Early Sci. J. China Univ. Geosci. 38 (5), 947–962.

Liu, B., Ma, C.Q., Jiang, H.A., Guo, P., Zhang, J.Y., Xiong, F.H., 2013a. Early Paleozoic tectonic transition from ocean subduction to collisional orogeny in the Eastern Kunlun region: evidence from Huxiaoqin mafic rocks. Acta Petrol. Sin. 29 (6), 2093–2106 (in Chinese with English abstract).

Liu, Y.S., Gao, S., Hu, Z.C., Gao, C.G., Zong, K.Q., Wang, D.B., 2010a. Continental and oceanic crust recycling-induced melt–peridotite interactions in the Trans-North China orogen: U–Pb dating, Hf isotopes and trace elements in zircons from mantle xenoliths. J. Petrol. 51 (1–2), 537–571.

Liu, S., Su, W.C., Hu, R.G., Feng, C.X., Gao, S., Coulson, I.M., Wang, T., Feng, G.Y., Tao, Y., Xia, Y., 2010b. Geochronological and geochemical constraints on the petrogenesis of alkaline ultramafic dykes from southwest Guizhou Province, SW China. Lithos 114, 253–264.

Lu, S.N., 2002. Precambrian Geology of the Northern Qinghai–Tibet Plateau. Geological Publishing House, Beijing, pp. 1–125 (in Chinese).

Lu, L., Zhang, Y.L., Wu, Z.H., Hu, D.G., 2013. Zircons U–Pb dating of early Paleozoic granites from the East Kunlun moutains and its geological significance. Acta Geosci. Sin. 34 (4), 447–454 (in Chinese with English abstract).

Ludwig, K.R., 2003. User's Manual for Isoplot 3.00: A Geochronological Toolkit for Microsoft Excel. Geochronology Center, Berkeley, pp. 1–70.

MacDonald, R., Rogers, N.W., Fitton, J.G., Black, S., Smith, M., 2001. Plume-lithosphere interactions in the generation of the basalts of the Kenya Rift, East Africa. J. Petrol. 42 (5), 877–900.

Mavrogenes, J.A., O'Neill, H.S., 1999. The relative effects of pressure, temperature and oxygen fugacity on the solubility of sulfide in mafic magmas. Geochim. Cosmochim. Acta 63 (7/8), 1173–1180.

Mckenzie, D., 1989. Cratonic, circumeratonic and oceanic mantle domains beneath the western United States. J. Geophys. Res. 94, 7899–7915.

Meng, F.C., Zhang, J.X., Cui, M.H., 2013. Discovery of Early Paleozoic eclogite from the East Kunlun, Western China and its tectonic significance. Gondwana Res. 23 (2), 825–836.

Menzies, M.A., 1990. Archaean, Proterozoic, and Phanerozoic lithospheres. In: Menzies, M.A. (Ed.), Continental mantle. Oxford Science Publications, New York, pp. 67–86.

Naldrett, A.J., 1989. Magmatic Sulfide Deposits. Oxford University Press, p. 196.

Naldrett, A.J., 2004. Magmatic Sulfide Deposits. Springer, Berlin, p. 727.

Neal, C.R., Mahoney, J.J., Chazey, W.J., 2002. Mantle sources and the highly variable role of continental lithosphere in basalt petrogenesis of the Kerguelen Plateau and Broken Ridge LIP: results from ODP Leg183. J. Petrol. 43, 1177–1205.

Pearce, J.A., 2008. Geochemical fingerprinting of oceanic basalts with applications to ophiolite classification and the search for Archean oceanic crust. Lithos 100 (1), 14–48.

Pearce, J.W., Peate, D.W., 1995. Tectonic implications of the composition of volcanic arc magmas. Annu. Rev. Earth Planet. Sci. 23, 251–285.

Qi, L., Hu, J., Gregoire, D.C., 2000. Determination of trace elements in granites by inductively coupled plasma mass spectrometry. Talanta 51 (3), 507–513.

Regelous, M., Collerson, K.D., Ewart, A., Wendt, J.I., 1997. Trace element transport rates in subbdction zones: evidence from Th, Sr and Pb isotope data for Tonga–Kermadec arc lavas. Earth Planet. Sci. Lett. 150, 291–302.

Ripley, E.M., 1981. Sulphur isotopic abundances of the Dunka Road Cu–Ni deposit, Duluth Complex, Minnesota. Econ. Geol. 76, 619–620.

Ripley, E.M., Park, Y.R., Li, C.S., Naldrett, A.J., 1999. Sulfur and oxygen isotopic evidence of country rock contamination in the Voisey's Bay Ni–Cu–Co deposit, Labrador, Canada. Lithos 47, 53–68.

Saunders, A.D., Norry, M.J., Tarney, J., 1988. Origin of MORB and chemically depleted mantle reservoirs: trace element constrains. Journal of Petrology (Special Lithosphere Issue) 425–445.

Sun, F.Y., Li, B.L., 2012. Work Program of Study on the Issue That Explore Metallogenic Belt in Qaidam Peripheral and Adjacent Regions(Restricted Data).

Sun, S.S., McDonough, W.F., 1989. Chemical and isotopic systematics of oceanic basalts: implications for mantle composition and processes. In: Saunders, A.D., Norry, M.J. (Eds.), Magmatism in Oceanic Basins. Spec. Publ. Geol Soc. Lond. 42, pp. 313–345.

Sun, F.Y., Chen, G.H., Chi, Q.G., 2003. Report of metallogenic regularity and prospecting direction comprehensive study in Xinjiang–East Kunlun metallogenic belt (in Chinese).

Tang, Z.L., Yan, H.Q., Jiao, J.G., Pan, Z.J., 2007. Regional metallogenic controls of small intrusion hosted Ni–Cu(PGE) ore deposits in China. Earth Sci. Front. 14 (5), 92–103 (in Chinese with English abstract).

Tian, L.Y., Castillo, P.R., Hilton, D.R., 2011. Major and trace element and Sr–Nd isotope signatures of the northern Lau Basin lavas: implications for the composition and dynamics of the back-arc mantle. J. Geophys. Res. 116. http://dx.doi.org/10.1029/2011JB008791.

Wang, G., 2014a. Metallogenesis of Nickel deposits in Eastern Kunlun Orogenic Belt, Qinghai Province. Jilin University, Changchun, pp. 1–200 (in Chinese with English abstract).

Wang, K.L., Chung, S.L., O'Reilly, S.Y., Sun, S.S., Shinjo, R., Chen, C.H., 2004. Geochemical constraints for the genesis of post-collisional magmatism and the geodynamic evolution of the northern Taiwan region. J. Petrol. 45 (5), 975–1011.

Wang, G., Sun, F.Y., Li, B.L., Li, S.J., Zhao, J.W., Ao, C., Yang, Q.A., 2014a. Zircon U–Pb geochronology and geochemistry of the mafic–ultramafic intrusion in Xiarihamu Cu–Ni deposit from East Kunlun, with implications for geodynamic setting. Earth Sci. Front. 21 (6), 381–401 (in Chinese with English abstract).

Wang, G., Sun, F.Y., Li, B.L., Li, S.J., Zhao, J.W., Yang, Q.A., 2014b. Zircon U–Pb geochronology and geochemistry of diorite in Xiarihamu ore district from East Kunlun, and its geological significance. J. Jilin Univ. (Earth Sci. Ed.) 44 (3), 876–891 (in Chinese with English abstract).

Wang, G., Sun, F.Y., Li, B.L., Li, S.J., Zhao, J.W., Yang, Q.A., Ao, C., 2013. Zircon U-Pb geochronology and geochemistry of the Early Devonian syenogranite in the Xiarihamu ore district from East Kunlun, with implications for the geodynamic setting. Geotecton. Metallog. 37 (4), 685–697 (in Chinese with English abstract).

Wang, C.Y., Zhou, M.F., 2006. Genesis of the Permian Baimazhai magmatic Ni–Cu–(PGE) sulfide deposit, Yunnan, SW China. Mineral. Deposita 41, 771–783.

Woodhead, J.D., Hergt, J.M., Davidson, J.P., Eggins, S.M., 2001. Hafnium isotope evidence for 'conservative' element mobility during subduction zone processes. Earth Planet. Sci. Lett. 192 (3), 331–346.

Wu, L.R., 1963. Metallogenic specialization of mafic, ultramafic rocks of China. Sci. Geol. Sin. 1, 29–41 (in Chinese).

Wu, F.Y., Li, X.H., Yang, J.H., Zheng, Y.F., 2007. Discussions on the petrogenesis of granites. Acta Petrol. Sin. 23 (6), 1217–1238 (in Chinese with English abstract).

Wu, F.Y., Simon, A.W., Zhang, G.L., Sun, D.Y., 2004. Geochronology and petrogenesis of the post-orogenic Cu–Ni sulfide-bearing mafic–ultramafic complexes in JiLin Province, NE China. J. Asian Earth Sci. 23, 781–797.

Xiao, X.C., Li, T.D., 2000. Tectonic Evolution and Uplift of Qinghai-Xizang Plateau. Guandong Science & Technology Press, Guangzhou (in Chinese).

Xu, Z.Q., 2006. Continental Dynamics of Qinghai–Xizang Plateau. Geological Publishing House, Beijing (in Chinese with English abstract).

Xu, Z.Q., Yang, J.S., Cheng, F.Y., 1996. The A'nyemaqen suture zone and the dynamics in subduction and collision. In: Qi, Z. (Ed.), Study on Ophiolites and Geodynamics. Geological Publishing House, Beijing, pp. 185–189 (in Chinese).

Yang, J.S., Robinson, P.T., Jiang, C.F., Xu, Z.Q., 1996. Ophiolites of the Kunlun Mountains, China and their tectonic implications. Tectonophysics 258 (1), 215–231.

Yuan, W.M., Mo, X.X., Wang, S.C., Zhang, X.T., 2003. The relationship between gold mineralization and regional tectonic evolution in the Eastern Kunlun Mountains. Geol. Prospect. 39 (3), 5–8 (in Chinese with English abstract).

Zhang, Z.C., Mao, J.W., Chai, F.M., Yan, S.H., Chen, B.L., Pirajno, F., 2009b. Geochemistry of the Permian Kalatongke mafic intrusions, Northern Xinjiang, NW China: implications for the genesis of the magmatic Ni–Cu sulfide deposit. Econ. Geol. 104, 185–203.

Zhang, Z.C., Mao, J.W., Saunders, A.D., Ai, Y., Li, Y., Zhao, L, 2009a. Petrogenetic modeling of three mafic–ultramafic layered intrusions in the Emeishan large igneous province, SW China, based on isotopic and bulk chemical constraints. Lithos 113, 369–392.

Zhang, D.Q., Dang, X.Y., She, H.Q., Li, H.Q., Li, D.X., Feng, C.Y., Li, J.W., 2005. Ar–Ar dating of orogenic gold deposits in northern margin of Qaidam and East Kunlun Mountains and its geological significance. Mineral Deposits 24 (2), 87–98 (in Chinese with English abstract).

Zhang, H.F., Sun, M., Lu, F.X., Zhou, X.H., Zhou, M.F., Liu, Y.S., Zhang, G.H., 2001. Geochemical significance of a garnet lherzolite from the Dahongshan kimberlite, Yangtze Craton, southern China. Geochem. J. 35, 315–331 (in Chinese with English abstract).

Zhang, Z.C., Yan, S.H., Chen, B.L., He, L.X., He, Y.S., Zhou, G., 2003. Geochemistry of the Kalatongke basic comples in Xinjiang and its constraints on genesis of the deposit. Acta Petrol. Mineral. 22 (3), 217–224 (in Chinese with English abstract).

Zindler, A., Hart, S.R., 1986. Chemical dynamics. Ann. Rev. Earth Planet. Sci. Lett. 14, 493–571.